Analysis of slip-weakening frictional laws with static restrengthening and their implications on the scaling, asymmetry, and mode of dynamic rupture on homogeneous and bimaterial interfaces

L. M. Olsen-Kettle,[1] D. Weatherley,[1] E. Saez,[1] L. Gross,[1] H.-B. Mühlhaus,[1] and H. L. Xing[1]

[1] Dynamic simulations of homogeneous, heterogeneous and bimaterial fault rupture using modified slip-weakening frictional laws with static restrengthening are presented giving rise to both crack-like and pulse-like rupture. We demonstrate that pulse-like rupture is possible by making a modification of classical slip-weakening friction to include static restrengthening. We employ various slip-weakening frictional laws to examine their effect on the resulting earthquake rupture speed, size and mode. More complex rupture characteristics were produced with more strongly slip-weakening frictional laws, and the degree of slip-weakening had to be finely tuned to reproduce realistic earthquake rupture characteristics. Rupture propagation on a fault is controlled by the constitutive properties of the fault. We provide benchmark tests of our method against other reported solutions in the literature. We demonstrate the applicability of our elastoplastic fault model for modeling dynamic rupture and wave propagation in fault systems, and the rich array of dynamic properties produced by our elastoplastic finite element fault model. These are governed by a number of model parameters including: the spatial heterogeneity and material contrast across the fault, the fault strength, and not least of all the frictional law employed. Asymmetric bilateral fault rupture was produced for the bimaterial case, where the degree of material contrast influenced the rupture speed in the different propagation directions.

1. Introduction

[2] Friction between solid interfaces is a key component in solid dynamics over a wide range of length scales: from the mechanics of earthquakes to machinery. When two solids are forced together their relative motion usually proceeds with jerky oscillations, in a cycle termed "stick-slip". The stick phase corresponds to the elastic loading of the system and a sudden slip is associated with the stress-relaxation of the system. Stick-slip occurs in many systems and earthquakes are an example of the stick-slip instability [*Baumberger et al.*, 1994]. The mechanism for the stick-slip instability can be described using various frictional laws [*Dieterich*, 1979; *Ruina*, 1983; *Madariaga et al.*, 1998]. Rate and state friction formulations are widely used to describe laboratory observations of frictional properties. However, the underlying physics controlling the rate and state dependent rock friction has been difficult to ascertain, and the parameters of these laws remain empirical and hard to extrapolate outside the laboratory range of conditions [*Marone and B. E. Hobbs*, 1992; *Marone*, 1998]. We adopted several forms of modified linear and nonlinear slip-weakening frictional laws and found that they produced a rich array of dynamical behavior during rupture at the fault. We modified classical slip-weakening friction [*Palmer and Rice*, 1973; *Ida*, 1972; *Andrews*, 1976] to include static restrengthening. Static restrengthening was initiated when a point on the fault was no longer slipping inelastically and the medium had relaxed around that point. This approach is distinct to other rate-dependent frictional laws where static restrengthening is initiated once the velocity has fallen below some threshold. The presence of restrengthening can reproduce in a very simplified manner the experimentally observed strong rate-dependence of frictional resistance.

[3] We consider both linear and nonlinear slip-weakening frictional laws. The use of nonlinear slip-weakening laws has already been advocated by several authors on the basis of purely seismic considerations [*Chambon et al.*, 2006, *Abercrombie and Rice*, 2005; *Rice and Cocco*, 2007;

[1]Earth Systems Science Computational Centre, The University of Queensland, St Lucia, Queensland, Australia.

Wibberley and Shimamoto, 2005; *Rice*, 2006; *Rice et al.*, 2005]. Given that earthquake slips are often accommodated within thin zones where evidence of melting is not pervasive especially at shallow depths, it is reasonable to expect that strong slip-weakening mechanisms must exist during rapid, large slip. A combination of observations and theory have led to several proposed mechanisms, including: rapid onset of slip but not necessarily large slip and strong rate-weakening which induces a self-healing pulse-like rupture mode [*Rice and Cocco*, 2007]. Employment of more strongly nonlinear slip-weakening laws in this work reproduced both of these mechanisms: rapid onset of slip at the beginning of the rupture and smaller average slips resulting overall, and in some cases pulse-like rupture could occur with these laws. Pulse-like rupture is possible in our models because we use modified slip-weakening laws with static restrengthening. This is an important distinction in our model from other purely slip-dependent frictional laws.

[4] Nonlinear slip-weakening laws have a multiscale character not envisioned in classical formulations of slip-weakening. The multiscale nature implies that discernible weakening continues at an ever-diminishing rate with slip. Such a response when fitted to classical linear slip-weakening laws has led instead to the interpretation that the characteristic slip distance (D_b in this paper) used in these linear laws depends on the slip in an earthquake. As the average slip scales with the rupture length, this characteristic distance should also scale with the earthquake size. *Wibberley and Shimamoto* [2005] considered exponential slip-weakening with varying characteristic slip distances. Other authors have also considered an exponential dependence on slip [*Lachenbruch*, 1980; *Mase and Smith*, 1987; *Rice et al.*, 2005]. Experimental and seismic evidence for strong slip-weakening mechanisms led us to explore laws with power law dependence on the slip in this paper.

[5] In section 2 we describe the finite element method we use based on the penalty method for contact problems with friction [*Perić and Owen*, 1992; *Laursen and Simo*, 1993; *Wriggers*, 2006] and define the different slip-weakening frictional laws we employed. In section 3 we describe the numerical time integration scheme employed for this work: a semi-implicit Gear algorithm [*Gear*, 1971]. Section 4 describes the numerical method used to model the two phases: first the quasi-static tectonic loading of the system, and secondly the dynamic rupture event. We present results for rupture of a fault in a homogeneous medium in section 5, and explore the conditions giving rise to either crack-like or pulse-like rupture. Section 6 presents similar results for bimaterial, heterogeneous fault rupture where we investigate the effect of varying material contrast across the interface on the bilateral asymmetric nature of rupture propagation. Finally, we summarize our major findings in section 7.

[6] We compare the results of our numerical simulations with laboratory findings, [*Xia et al.*, 2004, 2005; *Xia*, 2005; *Lykotrafitis et al.*, 2006; *Lykotrafitis and Rosakis*, 2006] geological observations of earthquakes [*Mai and Beroza*, 2000; *Heaton*, 1990; *Kanamori et al.* [1998]; *Harris and Day*, 2005; *Dor et al.*, 2006] and other theoretical and numerical work [*Harris and Day*, 2005, 1997; *Harris and Archuleta*, 2004; *Ben-Zion*, 2001; *Shi and Ben-Zion*, 2006; *Andrews and Ben-Zion*, 1997; *Day et al.*, 2005; *Rojas et al.*, 2008; *Ampuero and Ben-Zion*, 2007]. Our simulations shed

further light on current issues such as: bilateral versus unilateral rupture along bimaterial interfaces and the crack-like versus pulse-like nature of rupture propagation. These issues have important implications in understanding and simulating earthquake dynamics.

2. Elasto-Plastic Fault Model

[7] Deformation of a solid body in contact with a stiffer frictional constraint poses a challenging problem in continuum mechanics, and is relevant to a broad range of applications in mechanical and civil engineering, in addition to earthquake dynamics and faulting applications in geophysics. In this paper we utilize concepts of nonassociated elasto-plasticity for the construction of the constitutive equations for a frictional interface on a fault, and provide an integrated approach to modeling the mechanism of slip and rupture at a fault. We describe various forms of slip-weakening frictional laws based on the Coulomb failure criteria and apply these laws in the context of nonassociated elasto-plasticity theory [*Michalowski and Mròz*, 1978; *de Borst and Sluys*, 2002; *Perić and Owen*, 1992; *Wriggers et al.*, 1990; *Giannakopoulos*, 1989]. Other authors have also been successful in formulating friction at homogeneous interfaces using concepts from elasto-plasticity [*Coker et al.*, 2005; *Povirk and Needleman*, 1993].

[8] Modeling interface friction between two bodies in contact is a very complicated process. Many theories exist to describe the frictional resistance between two surfaces. The major factors contributing to the frictional resistance can be summarized qualitatively as: the effects of interlocking asperities, elastic-plastic deformation and fracture of the asperities, intense plastic deformation of the near-surface layers of the contact surface, and adhesion of newly created surfaces [*Anand*, 1993]. We develop a macroscopic continuum model for slip evolution during rupture at a fault that incorporates some of these microscopic factors through model parameters. In natural faults other complex factors can also contribute to the faulting process: melting, thermal fluid pressurization and lubrication [*Andrews*, 2002; *Kanamori and Brodsky*, 2004; *Wibberley and Shimamoto*, 2005; *Rice*, 2006; *Chambon et al.*, 2006; *Harris*, 2004].

[9] In general, finite element treatments of contact problems are divided between the penalty method and the method of Lagrange multipliers. When treating frictional problems the penalty method allows us to exploit the analogy between friction and plasticity in deriving the incremental tractions at the fault. The elastic stiffness moduli which characterize the relative motion of the fault interfaces are very high, acting effectively as penalty parameters. The elasto-plastic character of the deformation of the interfaces can be justified in relation to the deformation of the asperities on the contact interfaces, which consists of an elastic component, plastic deformation, damage and fracture [*Anand*, 1993; *Laursen and Simo*, 1993]. We are considering the interface friction between two fault surfaces where the predominant plastic slip is tangential to the fault. We study numerical solutions of the 2D wave equation where the penalty method is used to enforce the contact boundary conditions. The penalty method was also employed by *Coker et al.* [2005], *Povirk and Needleman* [1993], and *Shi et al.* [2008] in their implementation of
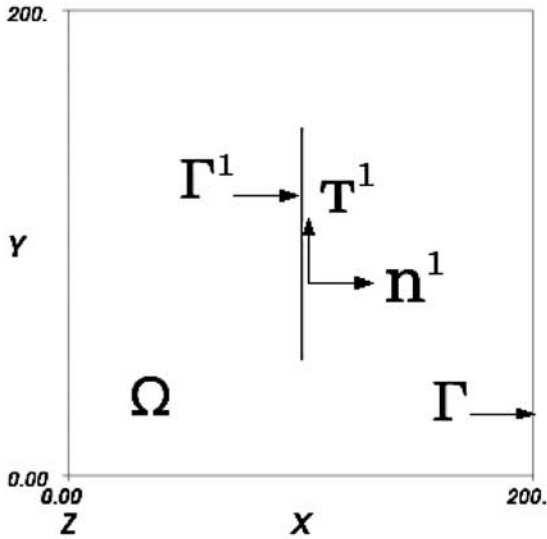
Figure 1. 2D fault model.

elasto-plasticity at homogeneous interfaces. We extend these results and apply the penalty method to bimaterial interfaces as well.

2.1. Numerical Model

[10] We study numerical solutions of the 2D wave equation in the region Ω (see Figure 1):

$$\rho \ddot{u}_i(t) = \sigma_{ij,j} + F_i, \tag{1}$$

where we are using Einstein notation. We solve the above wave equation using the finite element method and a second order four-valued semi-implicit Gear algorithm for the time integration [*Gear*, 1971]. Here u is the displacement vector field and the double dot above u implies second order differentiation with respect to time, ρ is the density of the elastic medium, F is a body force vector field, and σ_{ij} is the stress tensor field which in case of an isotropic, linear elastic material is given by:

$$\sigma_{ij} = \lambda u_{k,k} \delta_{ij} + \mu(u_{i,j} + u_{j,i}), \tag{2}$$

where λ and μ are the Lamé coefficients. We are solving this wave equation subject to slip boundary conditions on the fault, Γ^1 (see Figure 1):

$$\sigma_{ij} n_j^1 = F_n n_j^1 + F_\tau \tau_j^1 \quad \text{on} \quad \Gamma^1, \tag{3}$$

where n^1 and τ^1 are normal and tangential vectors to the fault (contact surface Γ^1).

[11] We define the tractions F_n and F_τ using the penalty method which employs elastic stiffness moduli (or penalty parameters), E_n and E_τ, to model the contact boundary conditions (discussed in section 2.2). The fault contact elements are modeled using zero-thickness joint elements where the displacements across the fault can be discontin-

uous. This approach is similar to the traction-at-split-node method [*Day et al.*, 2005; *Andrews*, 1999; *Rojas et al.*, 2008] where the fault is represented as a surface or line discretized by a set of double nodes called split nodes. Each half of the split node belongs to only one side of the fault and may experience motion relative to its counterpart. Thus the displacement can be discontinuous across the fault, this displacement discontinuity is usually termed the "slip" in seismology and fault mechanics. However, we use elasto-plasticity theory to decompose this relative displacement into an elastic plus plastic component, where we regard the plastic component as the "slip". In an analogous fashion the stress-glut method [*Dalguer and Day*, 2006] decomposes the strain rate into an elastic and inelastic component. The inelastic strain rate then defines the inelastic (or plastic) slip across the fault.

2.2. Interfacial Contact Constitutive Equations

[12] We implement plasticity at the fault interface, Γ^1, through the tractions, F_n and F_τ, which are defined using a combination of frictional constitutive laws and the penalty method. F_n and F_τ consider the coupling between the normal and tangential behavior of the slip, in addition to the loading of the system through strain at its external boundaries. F_τ acts tangential to the fault to prevent slip from occurring. F_n is a restoring force given by the penalty method to prevent the two sides from overlapping (the impenetrability condition). Thus we implement the penalty method to enforce these constraints and derive a constitutive law in the following equations which relates contact tractions to relevant kinematic quantities. This treatment of the frictional response of the fault is directly analogous to strain-driven algorithms for elastoplasticity [*Perić and Owen*, 1992; *Wriggers et al.*, 1990; *Giannakopoulos*, 1989].

[13] We can determine the tractions on the fault incrementally by adopting the following concepts from elasto-plasticity theory. In the elastoplastic model it is assumed that the relative displacement across the fault ($\tilde{u}$) can be split into an elastic ($\tilde{u}^e$) and a plastic component ($\tilde{u}^p$), i.e., $\tilde{u} = \tilde{u}^e + \tilde{u}^p$ [*de Borst and Sluys*, 2002; *Perić and Owen*, 1992; *Anand*, 1993; *Radi et al.*, 1999]. The relative displacement is defined as the difference in the displacements on either side of the fault contact surface, $\tilde{u} = u^1 - u^0$, where u^1 and u^0 are the displacements on either side of the fault surface. The elastic behavior is governed by the relationship:

$$\begin{pmatrix} \dot{F}_n \\ \dot{F}_\tau \end{pmatrix} = \begin{pmatrix} -E_n & 0 \\ 0 & -E_\tau \end{pmatrix} \begin{pmatrix} \dot{\tilde{u}}_n^e \\ \dot{\tilde{u}}_\tau^e \end{pmatrix},$$
$$= \begin{pmatrix} -E_n & 0 \\ 0 & -E_\tau \end{pmatrix} \begin{pmatrix} \dot{\tilde{u}}_n - \dot{\tilde{u}}_n^p \\ \dot{\tilde{u}}_\tau - \dot{\tilde{u}}_\tau^p \end{pmatrix},$$

where $\tilde{u}_n$ and $\tilde{u}_\tau$ are the relative normal and tangential displacements respectively and E_n and E_τ are the elastic stiffness constants (or penalty parameters). We assume that $\dot{\tilde{u}}_n^p = \beta(\tilde{u}_\tau^p) \dot{\tilde{u}}_\tau^p$ where β is the dilatancy factor [*Radi et al.*, 1999].

[14] The plasticity model is defined in terms of a Coulomb yield/failure function (ϕ), [*Perić and Owen*, 1992; *Giannakopoulos*, 1989; *Laursen and Simo*, 1993] separating the space of admissible from inadmissible stresses, and a flow rule which determines if plastic displace-

ment will occur once the yield criterion is met, as well as its magnitude and displacement. At each time step the incremental slip will have an elastic and plastic part determined by the yield criterion and flow rule for each point on the fault.

[15] We are using a Coulomb failure criterion to determine the yield surface for our problem. If the yield criterion is met for a point on the fault then plastic slip may occur and is determined such that the point will remain on the yield surface, $\phi = 0$ (consistency condition). However, if the yield criterion is not met then the point is in the elastic regime and only elastic slip will occur. Thus we need to determine if the Coulomb criterion is met at each time step, i.e., if $\phi = 0$ where ϕ is given below:

$$\phi = |F_\tau| + \mu_{fri}F_n - c \leq 0. \tag{4}$$

Here c is the cohesive factor and μ_{fri} is the coefficient of friction which can be either slip dependent or slip-rate dependent [*Marone and B. E. Hobbs*, 1992]. Here we restrict ourselves to defining the cohesion factor as a constant defined for each fault element and consider a slip dependent frictional coefficient, $\mu_{fri}(\tilde{u}_\tau^p)$.

[16] At each time step we need to test if the yield criterion, $\phi \leq 0$, is met. We achieve this using an elastic predictor, ϕ_{el}, where we assume at the next time step $(t + \delta t)$ the total incremental displacement is elastic (i.e., the incremental plastic slip is zero, $\delta\tilde{u}_\tau^p = 0$). ϕ_{el} is defined below:

$$\begin{aligned}
\phi_{el}^{t+\delta t} &= |F_\tau^{t+\delta t}| + \mu_{fri}^t F_n^{t+\delta t} - c^t, \\
&= |F_\tau^t + \delta t \dot{F}_\tau| + \mu_{fri}^t (F_n^t + \delta t \dot{F}_n) - c^t, \\
&= |F_\tau^t - E_\tau \delta\tilde{u}_\tau| + \mu_{fri}^t (F_n^t - E_n \delta\tilde{u}_n) - c^t,
\end{aligned}$$

where $\dot{\tilde{u}} = \delta\tilde{u}/\delta t$ and $\delta\tilde{u}$ is the incremental slip for that time step, and we expand the terms for the next time step, $t + \delta t$, as a first order Taylor expansion in t. If $\phi_{el}^{t+\delta t} \leq 0$ then the incremental plastic slip at that time step is zero, and consequentially $\phi_{el}^{t+\delta t} = \phi^{t+\delta t}$ and the yield criterion is met.

[17] For the case when $\phi_{el}^{t+\delta t} > 0$ we need to ensure that the yield criterion is met at each time step. We determine the incremental plastic slip such that $\phi^{t+\delta t} = 0$, i.e., ϕ remains on the yield surface if $\phi_{el}^{t+\delta t} > 0$ and equation (4) is satisfied.

$$\begin{aligned}
\phi^{t+\delta t} &= |F_\tau^{t+\delta t}| + \mu_{fri}^{t+\delta t} F_n^{t+\delta t} - c^{t+\delta t}, \\
&= (F_\tau^t - E_\tau \delta\tilde{u}_\tau)\chi + E_\tau |\delta\tilde{u}_\tau^p| \\
&\quad + \left(\mu_{fri}^t + \chi|\delta\tilde{u}_\tau^p|\frac{\partial\mu_{fri}}{\partial\tilde{u}_\tau^p}\right) \\
&\quad \cdot \left[F_n^t - E_n(\delta\tilde{u}_n - \beta^t|\delta\tilde{u}_\tau^p|)\right] - c^t - \chi|\delta\tilde{u}_\tau^p|\frac{\partial c^t}{\partial\tilde{u}_\tau^p}, \\
&= 0,
\end{aligned}$$

where $\chi = \text{sign}(F_\tau^t - E_\tau(\delta\tilde{u}_\tau - \delta\tilde{u}_\tau^p))$, and based on thermodynamic considerations, $\chi = \text{sign}(F^{t+\delta t}) = \text{sign}(\delta\tilde{u}_\tau^p)$. If we assume a point on the yield surface remains close to the yield surface, we can assume that $\chi = \text{sign}(F_\tau^{t+\delta t}) = \text{sign}(F_\tau^t)$.

[18] We consider a slip-dependent coefficient of friction, $\mu_{fri}(\tilde{u}_\tau^p)$ and assume $c(\tilde{u}_\tau^p)$ is also slip-dependent in the above equations. If we let $h^t = \chi(F_n^t \partial\mu_{fri}/\partial\tilde{u}_\tau^p - \partial c^t/\partial\tilde{u}_\tau^p)$ and

expand the above equation to first order in $|\delta\tilde{u}_\tau^p|$ we obtain the following equality for $\delta\tilde{u}_\tau^p$:

$$\delta\tilde{u}_\tau^p = \begin{cases} \dfrac{-\chi\Psi}{E_\tau + h^t + \mu_{fri}^t E_n \beta^t}, & \text{if } \phi_{el} > 0 \\[2mm] 0, & \text{if } \phi_{el} \leq 0 \end{cases},$$

where $\Psi = (F_\tau^t - E_\tau \delta\tilde{u}_\tau)\chi + \mu_{fri}^t(F_n^t - E_n\delta\tilde{u}_n) - c^t$

Thus we use the above definition of the plastic incremental slip at each time step to define the contact boundary condition at the next time step:

$$\sigma_{ij}n_j^1 = F_n n_j^1 + F_\tau \tau_j^1, \text{and } F_n^{t+\delta t} = F_n^t - E_n(\delta\tilde{u}_n - \beta^t|\delta\tilde{u}_\tau^p|),$$
$$F_\tau^{t+\delta t} = F_\tau^t - E_\tau(\delta\tilde{u}_\tau - \delta\tilde{u}_\tau^p).$$

2.3. Slip-Weakening Frictional Laws Considered

[19] The coefficient of friction (μ_{fri}) can be defined using various forms of slip-weakening and slip-rate weakening frictional laws. Two coefficients of friction are generally employed: the static coefficient of friction, μ_s, which governs the onset of slip, and a dynamic coefficient of friction, μ_d, which characterizes the behavior during sliding.

[20] We consider the following modified slip-weakening frictional laws:

$$\text{Linear:} \ \mu_{fri} = \begin{cases} \mu_s - (\mu_s - \mu_d)\dfrac{|s|}{D_b}, |s| < D_b, \mu_d, |s| \geq D_b. \end{cases} \tag{5}$$

$$\text{Cubic:} \ \mu_{fri} = \mu_d + (\mu_s - \mu_d)\frac{D_b^3}{(D_b + |s|)^3}. \tag{6}$$

$$\text{Quintic:} \ \mu_{fri} = \mu_d + (\mu_s - \mu_d)\frac{D_b^5}{(D_b + |s|)^5}. \tag{7}$$

$$\text{Septic:} \ \mu_{fri} = \mu_d + (\mu_s - \mu_d)\frac{D_b^7}{(D_b + |s|)^7}. \tag{8}$$

D_b is a characteristic slip distance for each law, and the above laws describe the frictional coefficient decreasing with slip on the fault, and are called slip-weakening in rock mechanics. The slip is defined as: $s = \tilde{u}_\tau^p(t) - \tilde{u}_\tau^p(t = \text{end of last slip event})$. Choosing to define the slip in this manner allows the fault to restrengthen to its initial frictional value after the rupture has terminated. Termination of a rupture event is determined dynamically for each point on the fault and occurs once a point is no longer slipping inelastically and is no longer yielding. Once the rupture event is over the frictional coefficient restrengthens to its initial value as $s = 0$ in this case. This presents a simple method to introduce a restrengthening mechanism that can reproduce the experimentally observed rapid healing of the fault. This is a crucial distinction from other purely slip-dependent frictional laws where there is no mechanism for the fault to heal and restrengthen to its static value of friction.
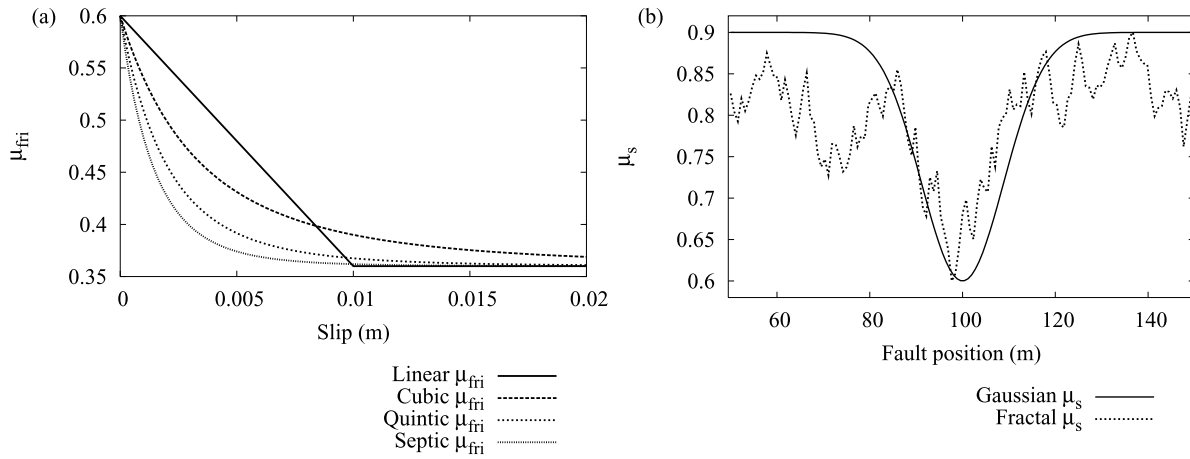
Figure 2. (a) Slip-weakening models for μ_{ffri} with $\mu_s = 0.6$ and $\mu_d = 0.6\ \mu_s$ and $D_b = 0.01$ m. (b) Different distributions for μ_s for modeling either a smooth (Gaussian well distribution) or rough fault (fractal distribution).

[21] The various forms of the slip-weakening laws above are plotted in Figure 2a. For small values of slip it is postulated that slip-weakening is the dominant feature, especially in rupture initiation. However, large values of slip typically exhibit slip-rate weakening characteristics [*Madariaga et al.*, 1998]. Frictional laws that incorporate both slip-rate dependence and memory (state) dependence have been successful in describing both laboratory friction data and observations from natural faults [*Dieterich*, 1979; *Ruina*, 1983]. However, implementation of these frictional laws requires additional integration of equations for the state variables. For our purpose we chose to use the above modified slip-weakening frictional laws in order to focus on the essential aspects of rupture propagation and the effect that the degree of slip-weakening in these laws has on the resulting earthquake rupture speed, size and mode. In principle any frictional constitutive law could be applied to our model with subsequent modifications to the above equations for the incremental plastic slip. For instance if a slip-rate weakening law is employed, the factor h (used in deriving the incremental plastic slip) would need to be modified to include the slip-rate dependence of μ_{ffri}.

[22] In the simulations for our fault we model μ_s as a function of fault position. Typically μ_s would vary according to multiple factors such as the effect of asperities on the fault, adhesion of contact surfaces etc. In the following simulations we use two simple models for μ_s (shown in Figure 2b). The first models μ_s as a Gaussian well for a smooth fault, with its minimum value at the midpoint of the fault, and the second provides a more realistic representation where a fractal distribution for μ_s is employed to simulate a rough fault (with its minimum value close to the midpoint of the fault). We vary the magnitude of μ_d in our simulations to observe how the weakness of the fault affects the rupture dynamics.

2.4. Weak Formulation of the Problem Using the Finite Element Method

[23] We are solving equation (1):

$$\rho \ddot{u}_i(t) = \sigma_{ij,j} + F_i,$$

subject to boundary conditions defined in equation (3):

$$\sigma_{ij}n_j = f_i \text{ on } \Gamma,$$
$$\sigma_{ij}n_j^1 = g_i \text{ on } \Gamma^1,$$

where Γ is the external surface and Γ^1 is the embedded fault surface.

[24] If we consider a function ω defined on our region Ω, then the weak formulation of equation (1) must satisfy:

$$\int_\Omega \omega_i \rho \ddot{u}_i(t) d\Omega = \int_\Omega \omega_i (\sigma_{ij,j} + F_i)\ d\Omega. \tag{9}$$

[25] We use Green's first identity to integrate the $\omega_i \sigma_{ij,j}$ term in equation (9) and obtain:

$$\int_\Omega \omega_i \sigma_{ij,j}\, d\Omega = -\int_\Omega \omega_{i,j}\sigma_{ij}\, d\Omega + \int_\Gamma \omega_i \sigma_{ij} n_j\, d\Gamma$$
$$+ \int_{\Gamma^1} \omega_i^1 \sigma_{ij}^1 n_j^1 d\Gamma^1 + \int_{\Gamma^1} \omega_i^0 \sigma_{ij}^0 n_j^0 d\Gamma^1. \tag{10}$$

[26] Using equation (10) and the boundary conditions combined with the fact that the normal stress is continuous at the fault, and defining $\tilde{\omega}_i = \omega_i^1 - \omega_i^0$, equation (9) becomes:

$$\int_\Omega \omega_i \rho \ddot{u}_i(t)\, d\Omega = -\int_\Omega \omega_{i,j}\sigma_{ij}\, d\Omega + \int_\Omega \omega_i F_i\, d\Omega$$
$$+ \int_\Gamma \omega_i f_i\, d\Gamma + \int_{\Gamma^1} \tilde{\omega}_i g_i\, d\Gamma^1.$$

[27] We solve the above equation using a parallel finite element library, Finley, which is part of an open source high level scripting language [*Gross et al.*, 2007].

3. Time Integration Scheme: Semi-Implicit Gear Algorithm

[28] The first step in the Gear algorithm is to use an explicit method to calculate the *predicted* displacements

(u_{pr}), velocities (v_{pr}) etc at the next time step ($t^{(n)}$) using the Taylor series:

$$u_{pr}^{(n)} = u^{(n-1)} + \delta t v^{(n-1)} + \frac{\delta t^2}{2} a^{(n-1)} + \frac{\delta t^3}{6} \dddot{u}^{(n-1)},$$

$$v_{pr}^{(n)} = v^{(n-1)} + \delta t a^{(n-1)} + \frac{\delta t^2}{2} \dddot{u}^{(n-1)},$$

$$a_{pr}^{(n)} = a^{(n-1)} + \delta t \dddot{u}^{(n-1)},$$

$$\dddot{u}_{pr}^{(n)} = \dddot{u}^{(n-1)}.$$

[29] These *predicted* displacements and velocities are used to calculate the *corrected* value for the acceleration at the next time step, $a^{(n)}$. This involves solving the dynamic wave equation (1) for the acceleration $a^{(n)}$ at the next time step $t^{(n)}$ subject to the boundary conditions previously outlined. Once we have obtained the acceleration at the next time step, we use this to update the solutions for the *corrected* displacements, velocities etc at the next time step.

[30] A 4-valued Gear algorithm is employed to calculate the *corrected* values for $u^{(n)}, v^{(n)}$ and $\dddot{u}^{(n)}$. First we define: $\Delta a = a^{(n)} - a_{pr}^{(n)}$, $c_0 = 1/6$, $c_1 = 5/6$, and $c_3 = 1/3$. We then evaluate the corrected values as follows: [*Gear*, 1971]

$$u^{(n)} = u_{pr}^{(n)} + c_0 \frac{\delta t^2}{2} \Delta a,$$

$$v^{(n)} = v_{pr}^{(n)} + c_1 \frac{\delta t}{2} \Delta a,$$

$$\dddot{u}^{(n)} = \dddot{u}_{pr}^{(n)} + c_3 \frac{3}{\delta t} \Delta a.$$

The Gear algorithm was used as it was the best compromise between accuracy and speed when compared to an explicit fourth order Runge Kutta method [*Press et al.*, 1992] which was slightly more accurate but also about four times more computationally expensive.

[31] Since we are modeling a fault in the Earth using a finite grid, we introduce absorbing boundary conditions for the acceleration at the grid edges to reduce the amplitude of the wave reflections at the external boundaries. This was achieved using the method of *Cerjan et al.* [1985], where the amplitude of the acceleration is gradually tapered from the physical interior boundary to the grid edges. In addition, we found that introducing an artificial viscosity term in the nonphysical boundary region acted to attenuate the waves further with time in this region. Since there is no viscosity in the physical modeling region a highly accurate solution for the wave propagation could be obtained. The artificial viscosity term is defined as $F_i = -\eta v_i$ in equation (1), and attenuates the wave velocities by a factor of $\exp(-\eta t/\rho)$ [*Mora and Place*, 1994]. We also imposed boundary conditions that the acceleration was vanishing at the external boundaries. These measures are taken so that subsequent reloading of the fault can occur after a rupture event has finished and multiple earthquake cycles can be simulated.

4. Tectonic Loading at the Fault

[32] Most earthquakes occur as the result of stress build-up at fault boundaries due to tectonic loading. When the stress due to tectonic loading has accumulated, such that the fault has reached its shear failure strength, it causes the fault to rupture in an earthquake. We modeled these stages independently in our numerical code: first we modeled the slow tectonic loading of the fault to failure quasi-statically, and secondly we modeled the dynamic rupture event and wave propagation when one point on the fault has reached its shear failure criterion and started to slip. This separation of the two processes has distinct computational advantages since it permits the simulation of multiple stick-slip cycles with greater ease and flexibility [*Olsen-Kettle et al.*, 2007]. This approach is different to that taken by *Lapusta et al.* [2000] and *Lapusta and Rice* [2003] where they allow slow tectonic loading of the fault with variable time stepping.

[33] We modeled the tectonic loading quasi-statically since tectonic loading rates are so small it would have been impractical to model the stress-loading dynamically. This quasi-static phase corresponds to the stick state where the system undergoes elastic loading and no plastic slip occurs. We emphasize that the method we use allows zero-velocity loading of the faults in contrast to many other numerical methods. Zero-velocity tectonic loading is appropriate for dynamic earthquake modeling because the tectonic strain rate is many orders of magnitude smaller than the transient strain rate due to seismic waves. We describe this phase in section 4.1. In section 4.2 we describe the dynamic rupture modeling.

4.1. Quasi-Static Loading

[34] In this section we describe the quasi-static method we used to implement tectonic loading of the fault and load the fault to failure. Tectonic loading of the fault is implemented by introducing strain at the external boundaries through compressing the domain boundaries normal to the fault and shearing the domain boundaries tangential to the fault. This is achieved using the analytic solution for the displacement with the applied external strains as the initial conditions:

$$u_x(t_0) = \epsilon_{00}\left(x - \frac{L}{2}\right),$$

$$u_y(t_0) = 2\epsilon_{01}\left(x - \frac{L}{2}\right),$$

where L is the length of one side of the domain and ϵ_{00} and ϵ_{01} are the applied external strains in the normal and tangential directions to the fault respectively. We then determined the magnitude of ϵ_{00} and ϵ_{01} required for the weakest point on the fault to reach failure and start to slip.

[35] The Coulomb failure criterion for a slip event to occur is when $|F_\tau| = -\mu_{fri}F_n + c$. At the fault we defined the following tractions for the boundary conditions in section 2.2 and equation (3):

$$\sigma_{ij}n_j^1 = F_n n_j^1 + F_\tau \tau_j^1$$

In our model n^1 is aligned with the x axis and τ^1 is aligned with the y axis (see Figure 1). Thus resolving equation (3) in

Table 1. Reproduction of Spontaneous Rupture Simulations of *Day et al.* [2005] and *Rojas et al.* [2008] for Different Mesh Resolutions and Using $E_n = E_\tau = (\lambda_1 + 2\mu_1/3)/100 \text{ m}^{-1}$[a]

Mesh Spacing, m	Time Step, s	RMS[b] Slip, m	RMS Peak Slip Velocity, m/s	Rupture Velocity, km/s	Rupture Time at $d = 12.5$ km, s
150	5e−3	5.82(−0.7%)[c]	4.72(29.3%)	3.06(2.7%)	4.03(−3.0%)
75	4.17e−3	5.83(−0.5%)	5.81(−12.9%)	3.01(0.9%)	4.12(−1.0%)
37.5	2.08e−3	5.86	6.68	2.98	4.16
			Rojas et al. [2008]		
12.5	1.04e−3	5.89	6.59		4.28

[a]In these simulations $\Lambda_0 = 1147.30$ m.
[b]RMS refers to the root mean square average.
[c]This percentage refers to the error misfit in these values with respect to the values obtained using the finest grid spacing (37.5 m).

the normal and tangential directions respectively, and using equation (2) and $\epsilon_{ij} = (u_{i,j} + u_{j,i})/2$ we obtain:

$$\epsilon_{00}(\lambda + 2\mu) = F_n, \qquad (11)$$

$$\epsilon_{01}(2\mu) = F_\tau. \qquad (12)$$

[36] Thus if $\lambda = \mu$ (a Poisson solid), we obtain a criterion for plastic slip to occur in terms of strain:

$$|\epsilon_{01}| = -\frac{3}{2}\mu_s\epsilon_{00} + \frac{c}{2\mu}. \qquad (13)$$

Here $\mu_{fri} = \mu_s$ for the quasi-static phase as no plastic slip occurs during this phase (i.e., $s = 0$ in equations (5) to (8)). During this phase we quasi-statically loaded the system to failure using the relationship between the external strains ϵ_{00} and ϵ_{01} defined in equation (13) above. We also increased the cohesive factor (c) so that no plastic slip occurred during the initial loading of the system. In the next stage dynamic rupture was initiated in a nucleation patch by modifying the cohesive factor in a region around the weakest point so that this point reaches failure.

[37] We can also evaluate equations (11) and (12) in terms of the elastic stiffness moduli (E_n and E_τ) we described in section 2.2:

$$\epsilon_{00}(\lambda + 2\mu) = F_n,$$
$$= -E_n\tilde{u}_n^e,$$
$$\text{or } \tilde{u}_n^e = -\epsilon_{00}\frac{(\lambda + 2\mu)}{E_n}$$

and:

$$\epsilon_{01}(2\mu) = F_\tau,$$
$$= -E_\tau\tilde{u}_\tau^e,$$
$$\text{or } \tilde{u}_\tau^e = -\epsilon_{01}\frac{(2\mu)}{E_\tau}.$$

The relationship between the strain and the tractions at the fault above demonstrates the effect of the elastic stiffness moduli (E_n and E_τ) on the normal and shear relative displacements at the fault ($\tilde{u}_n$, $\tilde{u}_\tau$ respectively). We also took advantage of the analytical solutions, $F_n^0 = (\lambda + 2\mu)\epsilon_{00}$ and $F_\tau^0 = 2\mu\epsilon_{01}$, and used these as initial conditions for F_n and F_τ to gain numerical convergence more rapidly and also to decrease the size of the overlap initially. By convention, E_n, $E_\tau > 0$ so that under compression ($\tilde{u}_n > 0$) the normal stress (F_n) is negative. As E_n, $E_\tau \to \infty$ the interface becomes

welded together, and the constraint conditions (zero relative slip) are satisfied [*Anand*, 1993; *Wriggers*, 2006]. Some authors have also interpreted the elastic moduli parameters as physical parameters describing the "shear" and "penetration" modulus of the interface. This issue remains unresolved and we simply model the elastic parameters as the maximum value that can be attained before numerical divergence of the solution occurs for the specified time step.

4.2. Dynamic Rupture

[38] In this stage we modeled the dynamic rupture event where one point on the fault has reached its shear failure strength and starts to slip. We used the numerical solutions obtained from the quasi-static loading phase as our initial conditions for the displacement, velocity etc. By modifying the cohesive factor (c) we can bring points on the fault closer to or further from failure. To initiate rupture at our loaded fault we lowered the cohesive factor in a nucleation patch centered at the weakest point of the fault so that at the first time step of the integration scheme it reaches its Coulomb failure strength and starts to slip. The cohesive factor was either lowered by a constant amount inside the nucleation patch (to reproduce the benchmark tests of *Day et al.* [2005], *Harris and Archuleta* [2004], and *Rojas et al.* [2008]) or variably (with the maximum amount at the weakest point and tapering off exponentially toward the edges of the nucleation patch). The cohesive factor was set to zero elsewhere on the fault.

[39] We study the evolution of dynamic rupture in the next two sections for both homogeneous and bimaterial interfaces with varying model parameters. For simplicity we did not consider dilatancy in the normal direction due to tangential slip in these calculations and set $\beta = 0$. We modeled the static coefficient of friction as a function of the position on the fault as shown in Figure 2b, and used either a Gaussian well distribution for a smooth fault or a fractal distribution for a rough fault. The dynamic coefficient of friction was modeled simply as a fraction of the static coefficient of friction: $\mu_d = \alpha\mu_s$, where α ranged from 0.2 to 0.9. We investigated the effect of material contrast across the fault in section 6 on the rupture propagation in different propagation directions and the extent of asymmetry in the displacement on either side of the fault.

5. Fault in a Homogeneous Medium

5.1. Spontaneous Rupture With a Linear Slip-Weakening Frictional Law and Constant μ_s

[40] In this part we reproduce the spontaneous rupture results reported by *Rojas et al.*, 2008 for 2D spontaneous
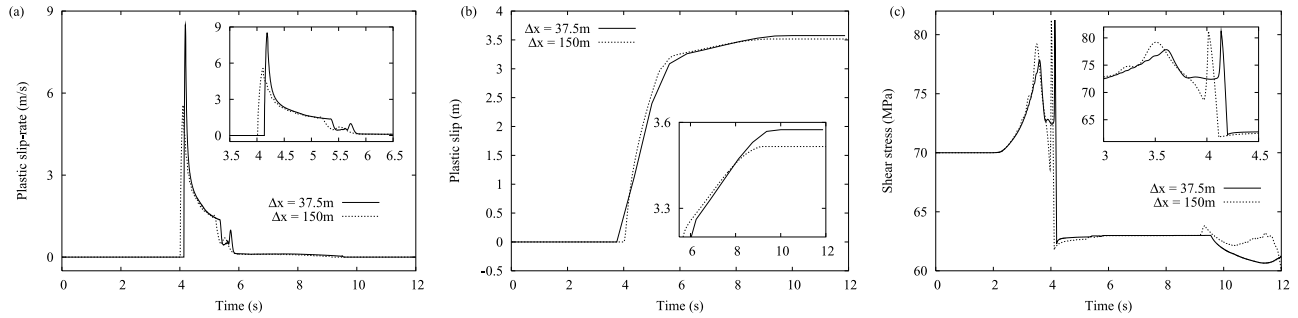
Figure 3. Time histories of the plastic slip-rate, plastic slip, and shear stress in Figures 3a, 3b, and 3c, respectively, for a point on the fault at a distance of approximately 12.5 km from the midpoint on the fault for two mesh spacings: $\Delta x = 37.5$ m and 150 m.

rupture and *Day et al.* [2005], *Harris and Archuleta* [2004] for 3D. We present results in this section for a 2D homogeneous fault model, using a 60×60 km^2 region (Ω) and fault length of 30 km, located at $x = 30$ km and from $y = 15$ km to 45 km in a similar fashion to the fault location in Figure 1. We used the following values for the Lamé coefficients: $\lambda = \mu = 32.04$ GPa and a density of $\rho = 2.67$ g/cm^3. Strains of $\epsilon_{00} = -0.00125$ and $\epsilon_{01} = 0.00109$ were applied, (these correspond to an initial normal stress of 120 MPa and an initial shear stress of 70 MPa). In this model the compressional wave speed is $V_p = 6$ km/s and the shear wave speed is Vs $= 3.46$ km/s.

[41] We used exactly the same parameters as *Rojas et al.* [2008] with a constant static and dynamic coefficient of friction: $\mu_s = 0.6$ and $\mu_d = 0.525$ (=0.875 μ_s) respectively. We used the linear slip-weakening frictional law shown in equation (5) with $D_b = 0.4$ m. A nucleation patch 3 km in size and centered around the midpoint of the fault was used (from $y = 28.5$ to 31.5 km). For failure to occur the Coulomb failure criterion must be met: $|F_\tau| = -\mu_{fri}F_n + c$, and in this model required $c = -11.24$ MPa in the nucleation patch. We further lowered the cohesive factor in this nucleation region by approximately 0.44% of the shear stress required for failure. This required lowering the cohesive factor uniformly in the nucleation patch to $c = -11.6$ MPa (instead of -11.24 MPa) to initiate rupture.

[42] Table 1 shows the numerical results our elastoplastic fault model produced for different mesh resolutions in order to show convergence of our results with increasing mesh resolution. We also show the results from *Rojas et al.* [2008] to directly compare their highest resolution results with our results. Rupture speeds were evaluated using a linear least squares analysis of the results [*Taylor*, 1982]. The rupture velocity refers to the evolution of the rupture front (when plastic slip first occurs at a point) with time. This definition of the speed of the rupture front is slightly different to that of *Rojas et al.* [2008] where they measure the rupture time as the time at which the slip velocity first exceeds 1 mm/s. This may explain why our rupture time at $d = 12.5$ km in Table 1 is smaller than the rupture time predicted by the model of *Rojas et al.* [2008].

[43] The parameter Λ_0 defined in this table is the same parameter as by *Day et al.* [2005] and is given by: $\Lambda_0 \approx C_1\mu/(F_n\frac{\partial\mu_{fric}}{\partial s}|_{s=0})$ where $C_1 \approx 9\pi/32$. Λ_0 is an upper-bound measure of the mesh resolution needed to accurately capture the "cohesive zone" during rupture. The cohesive zone is the portion of the fault length behind the crack tip where the shear stress decreases from its static value to its dynamic value.

[44] Figure 3 shows the slip-rate, slip and shear stress we obtained using a mesh spacing of either 37.5 m or 150 m at a distance of approximately 12.5 km from the midpoint on the fault. These plots are very similar to those of *Rojas et al.*
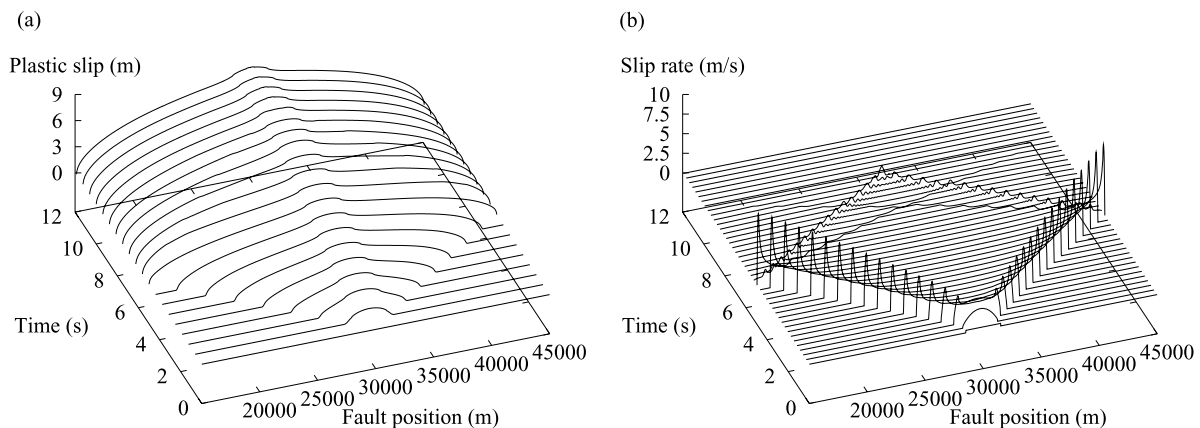

Figure 4. Time histories of the plastic slip along the fault and plastic slip-rate along the fault in Figures 4a and 4b respectively for a mesh spacing of $\Delta x = 37.5$ m.

Table 2. Results for Dynamic Simulations for Varying μ_d, μ_s and c Along a Fault in a Homogeneous Medium Using a Linear Slip-Weakening Law for μ_{fric} With $D_b = 0.01$ m and $E_n = E_\tau = (\lambda_1 + 2\mu_1/3)$ m^{-1a}

Parameters						Rupture velocity, km/s	
μ_d	Λ_0, m	Mesh spacing, m	Time step, $\times 10^{-5}$ s	RMS slip, cm	RMS Peak slip velocity, m/s	L	R
			Fractal μ_s, $c_{max} = 4.6\%$[b]				
$0.2\mu_s$	2.04	0.098	0.54	20.14	90.96	5.53	5.47
			Gaussian μ_s, $c_{max} = 2.3\%$[b]				
$0.5\mu_s$	3.27	0.098	0.54	8.69	23.55	2.83	
$0.51\mu_s$	3.34	0.20	1.09	8.29	21.07	2.75	
$0.52\mu_s$	3.41	0.20	1.09	7.79	19.55	2.72	
$0.53\mu_s$	3.48	0.20	1.09	0.06	2.09	creep event	

[a]A nucleation patch of 46.8 m for the fractal distribution of μ_s, and 7.8 m for the Gaussian distribution were used, where c was maximum ($=c_{max}$) at the weakest point in the center and exponentially decreasing toward the ends.
[b]At the weakest point c is lowered by this (maximum) percentage of the initial shear stress at the fault (129.6 MPa).

[2008] (see Figures 10 to 12) and *Day et al.* [2005] (see Figures 7 and 8). In Figure 4 we show time history surface plots of the slip and slip-rate along the fault for a mesh spacing of 37.5 m. The rupture velocity was subshear.

[45] However the resulting RMS (root mean square average) slip obtained here (>5 m) is anomalously high, compared to real earthquake scaling properties given by *Mai and Beroza* [2000], where a rupture length of 30 km generally implies a mean slip less than 1 m (at most). This anomaly led us to explore different forms of the slip-weakening law for μ_{fric} and to vary μ_s and μ_d in the next sections to observe the effect of these phenomena on the mode and scaling of rupture at the fault.

5.2. Spontaneous Rupture With Linear and Nonlinear Slip-Weakening Frictional Laws and Varying Distributions of μ_s

[46] We present results in this section for a fault in a homogeneous medium, using a 200 $\times$ 200 m^2 region (Ω) and fault length of 100 m, located at $x = 100$ m and from $y = 50$ to 150 m as shown in Figure 1. We used the following values for the Lamé coefficients: $\lambda = \mu = 36$ GPa and a density of $\rho = 3$ g/cm^3. Strains of $\epsilon_{00} = -0.002$ and $\epsilon_{01} = 0.0018$ were applied so that the weakest point on the fault is already at failure and equation (13) is satisfied. These correspond to an initial normal stress of 216 MPa and an initial shear stress of 129.6 MPa. The compressional wave speed is $V_p = 6$ km/s and the shear wave speed is $V_s = 3.46$ km/s. In section 6 we show results for a bimaterial fault model, i.e., a model with a contrast in the material properties across the fault.

[47] We present numerical results for the dynamic rupture along a fault in a homogeneous medium with varying fault parameters: the form of the slip-weakening law for μ_{fric} (Linear, Cubic, Quintic or Septic, see Figure 2a), the dynamic coefficient of friction, μ_d ($=\alpha\mu_s$), and for either a Gaussian well (smooth fault) or fractal (rough fault) distribution for μ_s (see Figure 2b).

5.2.1. Rupture With a Linear Slip-Weakening Frictional Law and Varying Distributions of μ_s

[48] Table 2 shows the numerical results for a Linear slip-weakening law for μ_{fric} (see equation (5) where $D_b = 0.01$ m). In Table 2 the letters L and R refer to the velocity of the rupture in the negative y direction and positive y direction respectively, since for the fractal distribution the slip will be asymmetric. Similarly to the experimental results of *Xia et al.* [2004] we found that the velocity of the rupture increases toward the P wave velocity as the fault weakens (lower μ_d) in Table 2. These numerical results confirm similar numerical [*Festa and Vilotte*, 2006] and theoretical [*Andrews*, 1976] studies where supershear crack-like rupture is observed as the magnitude of the dynamic strength drop increases (here this is due to the decrease in μ_d).

[49] The Linear slip-weakening law has the lowest slip-weakening rate considered of all the models. Consequently, much lower values of μ_d had to be used to for the rupture to propagate outside the nucleation region. For the fractal distribution of μ_s, c had to be lowered by twice the amount needed for the Gaussian distribution of μ_s, and over a much larger nucleation area. Using a fractal distribution of μ_s meant that the rupture could only break through the strong
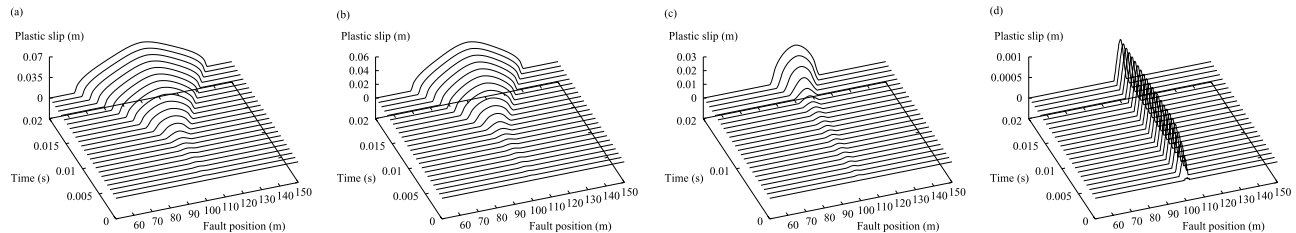

Figure 5. Rupture nucleation for varying fault strengths. Time histories of the plastic slip along the fault during rupture nucleation ($t < 0.02$ s) for a Linear slip-weakening law for μ_{fric}, a Gaussian distribution for μ_s, and $\mu_d = 0.5$ μ_s, 0.51 μ_s, 0.52 μ_s, and 0.53 μ_s in Figures 5a to 5d, respectively, using a mesh spacing of $\Delta x = 0.20$ m.
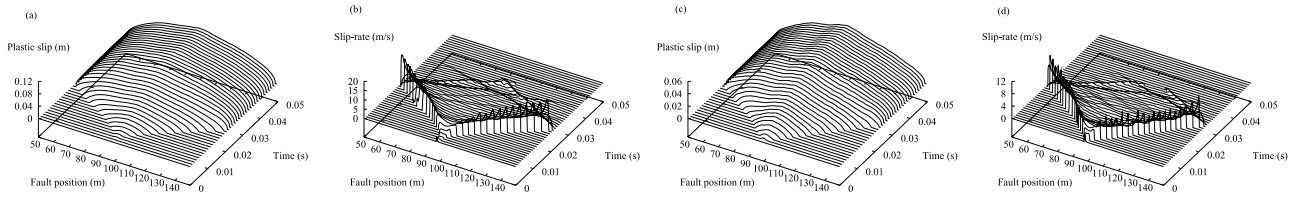
Figure 6. Sustained crack-like rupture plots. Time histories of the plastic slip and plastic slip-rate along the fault in Figures 6a and 6b respectively using a Cubic slip-weakening law for μ_{fric} and $\mu_d = 0.54 \ \mu_s$. Similar plots using a Quintic slip-weakening law for μ_{fric} and $\mu_d = 0.65 \ \mu_s$ in Figures 6c and 6d, respectively. All plots use a mesh spacing of $\Delta x = 0.39$ m.

regions of the fault (high μ_s) with a very low value of μ_d (=0.2 μ_s), and a strong nucleation event. These initial conditions meant that supershear rupture velocities and very large slip occurred for the fractal case. If a higher μ_d or smaller nucleation event were employed the resulting dynamic rupture for the fractal case was only a very small creep event (order of mm).

[50] In contrast when the Gaussian distribution of μ_s was implemented on the fault, the fault ruptured for higher values of μ_d and with a weaker nucleation event, resulting in subshear ruptures and smaller slip occurring at the fault. We also reported cases where the value of μ_d was just high enough that the dynamic event was only a small creep event with a RMS slip of approximately 0.7 mm. Figure 5 substantiates this claim where we see that as the fault strengthens (higher μ_d) the rupture nucleation event creeps for longer periods of time in (a) to (c) and eventually when μ_d is the highest in (d) the resulting rupture is only a small creep event (order of mm).

[51] The RMS slip, RMS peak slip velocity and rupture velocity converged with mesh size reduction as shown in Figure 11. Similarly to the results of *Rojas et al.* [2008] we found that the RMS slip and rupture velocity (or time in their case) converged the most rapidly, whereas the RMS peak slip velocity converged much more slowly.

[52] The rupture velocities for the Gaussian distribution of μ_s gave realistic subshear rupture velocities ranging between 79–82% of the shear wave speed. Most crustal

earthquakes have subshear wave speeds at approximately 70–80% of the shear wave speed [*Kanamori et al.*, 1998]. However, there are a few reported cases where the rupture velocity at least locally becomes supershear [*Xia et al.*, 2004; *Rice*, 2001; *Rosakis et al.*, 1999].

[53] However it is clear that using a Linear slip-weakening law with either distribution for μ_s gave resulting RMS slips (>8 cm) which are not realistic and much higher than mean slips (generally <2 cm) observed naturally for fault rupture lengths of 100 m [*Mai and Beroza*, 2000]. This led us to explore more strongly slip-weakening laws in the next section in an attempt to find the optimal slip-weakening law for rupture events with both realistic RMS slips and rupture velocities.

5.2.2. Rupture With Nonlinear Slip-Weakening Frictional Laws and a Heterogeneous (Fractal) Distribution of μ_s

[54] We used the same fault model as in 5.2.1, except in this section we always employed a fractal distribution for μ_s, and instead considered various forms for μ_{fric}: Cubic, Quintic and Septic (equations (6) to (8) with $D_b = 0.01$ m). Equations (6) to (8) become progressively more strongly slip-weakening.

[55] For the remainder of the calculations we used a nucleation patch of 7.8 m with the maximum value of c at the weakest point in the center of the nucleation patch, and considered the cohesive factor exponentially decreasing to zero toward the edge of the nucleation region. The cohesive

Table 3. Results for Dynamic Simulations Using Nonlinear Slip-Weakening Laws for μ_{fric} and Varying μ_d Along a Heterogeneous Fault (Fractal μ_s) in a Homogeneous Medium

μ_d	Λ_0, m	Mesh Spacing, m	Time Step, $\times 10^{-5}$s	RMS Slip, cm	RMS Peak Slip Velocity, m/s	Rupture Velocity, km/s L	R
			(a) Cubic Slip-Weakening Law for μ_{fric}				
$0.5\mu_s$	1.09	0.098	0.54	9.16	19.65	3.94[a]	2.96
$0.54\mu_s$	1.18	0.098	0.54	7.82	15.35	2.89	2.79
$0.56\mu_s$	1.24	0.20	1.09	7.00	12.10	2.67	2.58
$0.57\mu_s$	1.27	0.20	1.09	0.06	2.51	Creep event	
			(b) Quintic Slip-Weakening Law for μ_{fric}				
$0.65\mu_s$	0.93	0.098	0.54	3.86	10.63	2.51[a]	2.13
$0.68\mu_s$	1.02	0.098	0.54	2.48	5.23	1.85	0.92[a]
$0.69\mu_s$	1.06	0.39	2.17	1.49	3.29	1.00[a]	No rupture
$0.7\mu_s$	1.09	0.39	2.17	1.09	2.52	Middle segment only	
$0.72\mu_s$	1.17	0.39	2.17	0.06	1.29	Creep event	
			(c) Septic Slip-Weakening Law for μ_{fric}				
$0.68\mu_s$	0.73	0.098	0.54	2.79	14.55	2.52	1.65
$0.69\mu_s$	0.75	0.098	0.54	2.33	10.96	2.28	1.05[a]

[a]The rupture in this direction did not proceed in a constant fashion, this velocity is the straight line approximation to the rupture path.
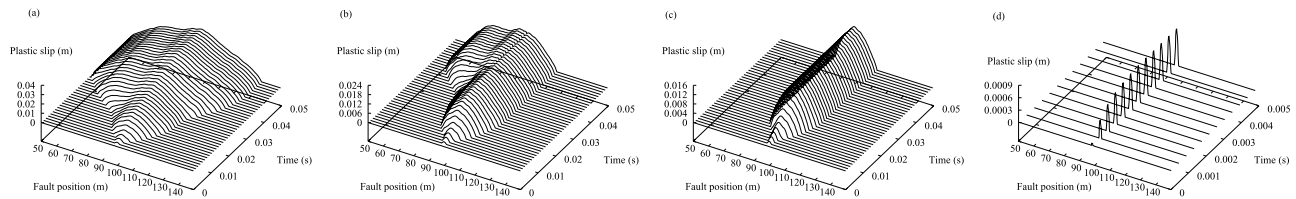
Figure 7. Varying degrees of decaying pulse-like rupture plots for progressively stronger faults from Figures 7a to 7d. Time histories of the plastic slip along the fault for a Quintic slip-weakening law for μ_{fric} and $\mu_d = 0.68$ μ_s, 0.69 μ_s, 0.7 μ_s, and 0.72 μ_s in Figures 7a to 7d, respectively, and a mesh spacing of $\Delta x = 0.39$ m.

factor was lowered to 2.3% of the initial shear stress ($c_{max} = 3$MPa) at the weakest point. Unless otherwise stated the penalty parameters employed for the remainder of the calculations are: $E_n = E_\tau = (\lambda_1 + 2\mu_1/3)$ m^{-1}.

[56] Table 3 shows results for different nonlinear slip-weakening laws for μ_{fric}: Cubic, Quintic and Septic slip-weakening respectively with varying μ_d. Table 3a still shows relatively high RMS slips (>6 cm) occurring for a range of μ_d using a Cubic law. Again we see that as in the Linear slip-weakening case the resulting rupture is either a sustained crack through the whole fault or a small creep event occurring in a very small patch on the fault. In contrast, we observe later that more strongly slip-weakening laws can produce either crack-like or pulse-like rupture depending on the weakness of the fault. Figures 6a and 6b also confirm the sustained crack-like nature of rupture propagation for the Cubic law, where the plastic slip and plastic slip-rate time histories are plotted along the fault. Sustained crack-like rupture propagation has been frequently reported for a fault in a homogeneous medium [*Andrews*, 1976; *Day et al.*, 2005].

[57] There are two widely accepted models of rupture in earthquake faulting: crack-like and pulse-like. Crack-like rupture is thought to occur mainly in homogeneous fault systems and as we demonstrate in this paper its formation also depends on the nature of the frictional law. Pulse-like ruptures is thought to usually occur in bimaterial fault systems where strong coupling between the normal and shear stress at the interface of the bimaterial aids in the development of a slip pulse. Pulse-like ruptures can also be present in homogeneous fault systems and can arise from certain conditions: spatial heterogeneities along the fault, strongly slip-weakening or slip-rate weakening friction, strengthening of the fault in stationary contact, and an optimum driving stress (which has to be lower than a certain value but high enough to allow self-sustained rupture propagation) [*Zheng and Rice*, 1998; *Lykotrafitis et al.*, 2006].

Pulse-like ruptures produce "self-healing" slip pulses that propagate along the fault, whereas in crack-like ruptures, the termination of the rupture front produces a backwards healing phase [*Xia*, 2005; *Heaton*, 1990; *Ben-Zion*, 2001; *Rice*, 2001]. This backwards healing phase can be readily observed in Figures 6b and 6d.

[58] In Figures 6c and 7 we show the different rupture modes observed for varying weakness of the fault (i.e., different values of μ_d) using a Quintic law. In Figure 6c a sustained crack-like rupture mode is observed for the weakest fault considered where $\mu_d = 0.65$ μ_s, whereas in Figures 7a to 7d varying degrees of decaying pulse-like rupture are observed for values of μ_d ranging from $\mu_d = 0.68$ μ_s to 0.72 μ_s. Decaying pulses have also been reported in homogeneous media [*Cochard and Madariaga*, 1994; *Zheng and Rice*, 1998; *Nielsen and Carlson*, 2000; *Ampuero and Ben-Zion*, 2007]. Crack-like, pulse-like and mixed rupture modes have been observed experimentally for homogeneous interfaces by *Lykotrafitis et al.* [2006] and *Lykotrafitis and Rosakis* [2006]. In their experimental study they concluded that pulse formation was mainly due to the velocity-weakening character of the frictional law or to changes in the frictional resistance by nonuniform variations in dynamic normal stress on the rupture interface, rather than due to spatial heterogeneities forming barriers to the rupture along the fault. In an analogous fashion our results also show that the degree of slip-weakening is also very important in the formation of pulses. Only the more strongly slip-weakening Quintic and Septic laws showed evidence of pulse-like rupture occurring, and this depended on μ_d falling in a critical range.

[59] We also demonstrate that the spatial heterogeneity of the fault is important in Figure 7b where the slip is terminated before it reaches one end of the fault (at $y = 150$ m). This is because μ_s is on average higher in this section and locks the fault. Figure 7b shows some evidence of pulse-like rupture propagation, where the midpoint has
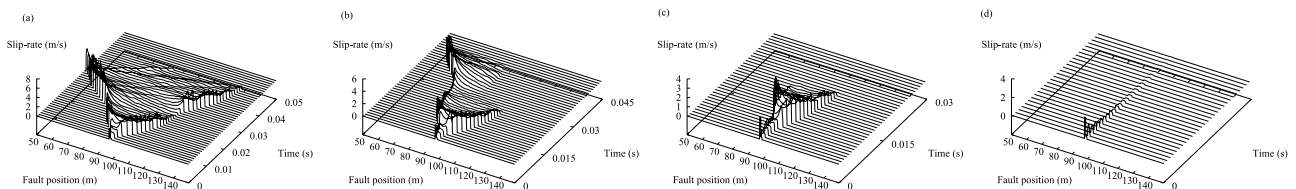

Figure 8. Time histories of the plastic slip-rate along the fault for progressively stronger faults from Figures 8a to 8d. The same parameters as Figure 7 were used: a Quintic slip-weakening law for μ_{fric} and $\mu_d = 0.68$ μ_s, 0.69 μ_s, 0.7 μ_s, and 0.72 μ_s in Figures 8a to 8d, respectively, and a mesh spacing of $\Delta x = 0.39$ m.
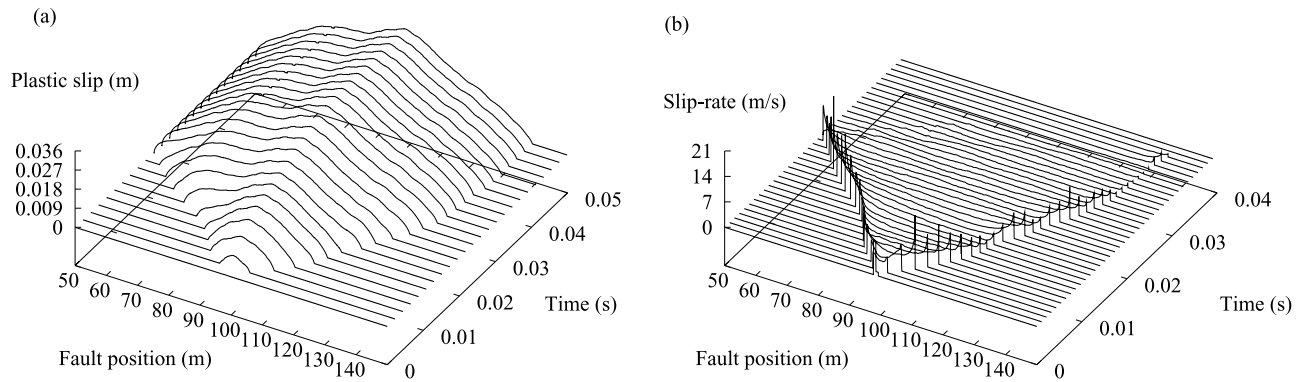
Figure 9. Time histories of the plastic slip and plastic slip-rate along a heterogeneous fault in a homogeneous medium in Figures 9a and 9b respectively for a Septic slip-weakening law for μ_{fric} and $\mu_d = 0.69 \; \mu_s$ and a mesh spacing of $\Delta x = 0.098$ m.

stopped slipping before other parts of the fault. This mechanism of short-duration, crack-like ruptures on small rupture regions (the barrier model) is one of the mechanisms proposed in forming slip-pulses [*Heaton*, 1990; *Ben-Zion*, 2001]. Other important factors that influence whether or not slip pulses are produced are: the degree of slip or slip-rate weakening in the frictional law as mentioned above, the heterogeneity of the fault, and the presence of a low-velocity fault core which separates two dissimilar rocks [*Xia*, 2005; *Heaton*, 1990; *Ben-Zion*, 2001; *Cochard and Madariaga*, 1994; *Ampuero and Ben-Zion*, 2007]. Finally we show cases where just the midsection of the fault ruptured in Figure 7c and a small creep event in 7d.

[60] Similarly Figures 8a to 8d show the corresponding time history plots of the slip-rate along the fault with a Quintic law and varying μ_d as in Figure 7. Backwards healing phases can be observed during rupture propagation in Figures 8a to 8c (where pulse-like rupture occurred) instead of predominantly after the rupture front reaches the ends of the faults as in Figures 6b and 6d (where sustained crack-like rupture occurred). Figures 8a to 8c also show that the fault ruptured in patches. *Lykotrafitis and Rosakis* [2006] also found experimentally that sliding areas in frictional interfaces could grow at various discrete speeds

without noticeable acceleration phases unlike classical sustained cracks in coherent interfaces.

[61] We compare results in Table 3b and 3c for a Quintic and Septic law respectively. Both the Quintic and Septic law proved to be strongly slip-weakening enough to produce a range of rupture modes from crack-like to pulse-like. Formation of pulse-like ruptures was also dependent on the magnitude of μ_d employed, where if it was too low, crack-like rupture resulted. A similar trend was also noted by *Festa and Vilotte* [2006] where they observed that pulse-like rupture was observed as the dynamic stress drop decreased (here this corresponds to an increase in μ_d).

[62] We found that smaller RMS slips were produced using the Quintic law for μ_{fric} than the corresponding Septic case where the same values of μ_d were used. RMS peak slip velocities were also smaller and closer to geological observations. Logarithmically averaged particle velocities on a fault were observed experimentally by *Heaton* [1990] to range from 0.4 to 1 m/s, but in the immediate vicinity of the rupture front were proposed to be in the order of $10-20$ m/s. The rupture velocities ranged from 53% to 72% of the shear wave speed for the Quintic law (in cases where the rupture path was approximately linear).

[63] Figures 9a and 9b show slip and slip-rate time history plots respectively along the fault using a Septic law. The
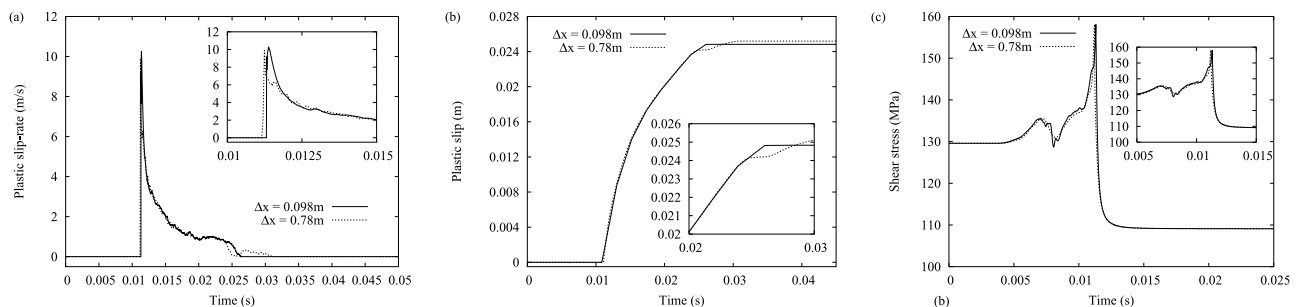

Figure 10. Time histories of the plastic slip-rate, plastic slip, and shear stress in Figures 10a, 10b, and 10c, respectively, for a point on the fault at a distance of approximately 25 m (at $y = 75$ m) from the midpoint on the fault for two mesh spacings: $\Delta x = 0.098$ m and 0.78 m. These plots were calculated for a Septic slip-weakening law for μ_{fric} and $\mu_d = 0.69 \; \mu_s$ and using a heterogeneous fault in a homogeneous medium.
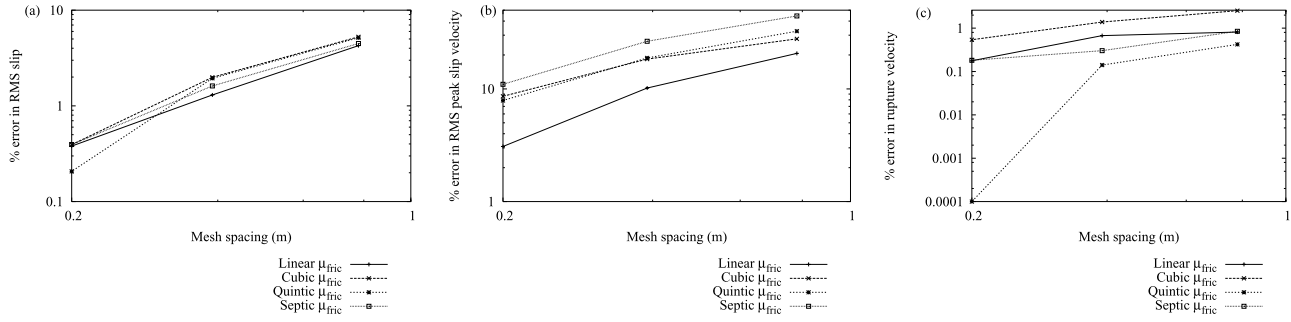
Figure 11. These plots show the percent error in RMS slip, RMS peak slip velocity and rupture velocity relative to the numerical solution for the finest mesh spacing (9.8 cm) in Figures 11a–11c, respectively. We show percent error for four different slip-weakening laws: linear μ_{fric} with a Gaussian distribution for μ_s and $\mu_d = 0.5\mu_s$ ($\Lambda_0 = 3.27$ m); the rest consider a fractal distribution for μ_s and rupture velocity in right direction (toward $y = 150$ m end). The error plots for the remaining three nonlinear laws consider: Cubic μ_{fric} and $\mu_d = 0.5\mu_s$ ($\Lambda_0 = 1.09$ m); Quintic μ_{fric} and $\mu_d = 0.65\mu_s$ ($\Lambda_0 = 0.93$ m); and Septic μ_{fric} and $\mu_d = 0.68\mu_s$ ($\Lambda_0 = 0.73$ m).

slip-rate time history plot shows evidence of a decaying pulse occurring in the R direction (from $y = 100$ to 150 m) and a sustained pulse in the L direction.

[64] Figures 10a to 10c show the slip-rate, slip and shear stress respectively for a point on the fault at $y = 75$ m (25 m from the midpoint of the fault). We show these for the strongest slip-weakening law: the Septic case (and thus also the smallest Λ_0 for cohesive zone resolution) and using a mesh spacing of either 0.098 m or 0.78 m. These plots also show that the numerical results converged with increasing mesh resolution, and the low level of numerical noise using our method. Figures 11a to 11c also show numerical convergence of the results for the linear and nonlinear laws considered where the percent error of the RMS slip, RMS peak slip velocity and rupture velocity are plotted.

[65] Overall we found that the Quintic law for μ_{fric} resulted in the most realistic RMS slips, peak slip velocities and rupture velocities. More complex rupture characteristics were produced with more strongly slip-weakening frictional laws. From this we can infer that the degree of slip-weakening in the frictional law is very relevant to the mode and scale of rupture produced, and has to be finely tuned to reproduce realistic earthquake rupture characteristics.

6. Bimaterial Fault Model

[66] Faults often separate rocks with different material and mechanical properties, estimates of velocity contrasts range from a few percent to as high as 30% in some regions [*Cochard and Rice*, 2000]. These material contrasts can lead to ramifications in earthquake dynamics which are investigated in this section.

[67] In the following two sections we employ a fractal distribution for μ_s and consider a Septic slip-weakening law for μ_{fric} again with $D_b = 0.01$ m and $\mu_d = 0.69 \mu_s$ in equation (8). We investigate the effect of varying material contrast across a bimaterial fault on the rupture velocity in

Table 4. Results for Dynamic Simulations Using a Septic Slip-Weakening Law for μ_{fric} and $\mu_d = 0.69 \mu_s$ Along a Bimaterial Fault With Varying Contrast in the Shear Wave Speeds Across the Fault[a]

μ_d Λ_0 Case	Mesh Spacing, m	Time Step, $\times 10^{-5}$s	RMS Slip, cm	RMS Peak Slip Velocity, m/s	Rupture Velocity, km/s	
					L	R
		(a) Bi-material Fault With 10% Contrast in Shear Wave Speeds Across Fault				
$\mu_d = 0.69\mu_s$	0.78	3.83	2.17(−1.9%)[b]	6.97(−44.2%)	2.44(−0.4%)	1.29(13.5%)[c]
$\Lambda_0 = 0.75$ m	0.39	1.91	2.21(0.0%)	9.17(−26.7%)	2.44(−0.3%)	1.25(10.1%)[c]
L-POS	0.20	0.96	2.23(0.5%)	11.08(−11.4%)	2.45(0.0%)	1.19(4.8%)[c]
	0.098	0.48	2.21	12.51	2.45	1.14[c]
L-NEG	0.098	0.48	2.21	9.89	2.27	1.38[c]
		(b) Bi-material Fault With 25% Constrast in Shear Wave Speeds Across Fault				
$\mu_d = 0.69\mu_s$	0.78	3.27	1.78(−2.7%)[b]	6.84(−50.3%)	2.46(−2.0%)	1.05(1.0%)[c]
$\Lambda_0 = 0.75$ m	0.39	1.63	1.81(−0.9%)	8.89(−35.4%)	2.49(1.0%)	1.05(1.2%)[c]
L-POS	0.20	0.82	1.82(−0.1%)	11.27(−18.1%)	2.49(−0.6%)	1.04(0.3%)[c]
	0.098	0.41	1.83	13.77	2.51	1.04[c]
L-NEG	0.098	0.41	1.71	7.40	1.82	1.10[c]

[a]We compared two simulations: first where L is in the direction of rupture in the positive direction (L-POS) to the case where L is in the direction of rupture in the negative direction (L-NEG).
[b]This percentage refers to the error misfit in these values with respect to the values obtained using the finest grid spacing (9.8 cm) for this simulation.
[c]The rupture in this direction did not proceed in a constant fashion, this velocity is the straight line approximation to the rupture path.

Region 1	Region 2
$\rho_1 = 3\,g/cm^3$	$\rho_2 = 2.5\,g/cm^3$
$\lambda_1 = 36\,GPa$	$\lambda_2 = 38.5\,GPa$
$\mu_1 = 36\,GPa$	$\mu_2 = 38.5\,GPa$
$V_s = 3.5\,km/s$	$V_s = 3.9\,km/s$
$V_p = 6\,km/s$	$V_p = 6.8\,km/s$

Figure 12. 2D bimaterial fault model.

either the positive (direction of slip in the more compliant material) and negative direction.

6.1. Rupture With 10% Contrast in the Shear Wave Speeds Across a Bimaterial Fault

[68] We present results in this section for a bimaterial, heterogeneous fault model, using a 200×200 m^2 region and fault length of 100 m. Figure 12 shows the values of the Lamé coefficients and density for the two regions, 1 and 2. The contrast in the shear wave speeds of the two materials is approximately 10%, where region 2 is the faster material with a shear wave speed of Vs = 3.93 km/s and a compressional wave speed of V_p = 6.8 km/s. Strains of $\epsilon_{00}^1 = -0.002$ and $\epsilon_{01}^1 = 0.0018$ ($\epsilon_{00}^2 = -0.001869$ and $\epsilon_{01}^2 = 0.001682$) are applied so that the midpoint on the fault is already at failure and equation (13) is satisfied. ϵ_{xy}^1 refers to the strain applied to region 1 and ϵ_{xy}^2 refers to the strain applied to region 2.

[69] Similarly to section 4.1 we define the Coulomb failure criteria for a rupture event to occur in terms of the strains. Since the normal stress is continuous on either side of the material interface: $\sigma_{ij}^1 n_j^1 = \sigma_{ij}^2 n_j^1$, where σ^1 is the stress for region 1 and similarly for σ^2. Thus the strains on either side of the interface are given by:

$$\epsilon_{00}^2 = \left(\frac{\lambda_1 + 2\mu_1}{\lambda_2 + 2\mu_2}\right)\epsilon_{00}^1, \epsilon_{01}^2 = \frac{\mu_1}{\mu_2}\epsilon_{01}^1,$$

and the initial displacements are given by:

$$u_x(t_0) = \begin{cases} \epsilon_{00}^1(x - L/2) & x \le L/2 \\ \\ \epsilon_{00}^2(x - L/2) & x > L/2 \end{cases},$$

$$u_y(t_0) = \begin{cases} 2\epsilon_{01}^1(x - L/2) & x \le L/2 \\ \\ 2\epsilon_{01}^2(x - L/2) & x > L/2 \end{cases}.$$

[70] Table 4a shows the results for a bimaterial, heterogeneous fault with 10% contrast in the shear wave speeds across the fault. We investigated the difference in bimaterial fault rupture along either the positive direction, (the direction of slip in the more compliant material), or in the negative direction. We compared the following two simu-

lations with the fault in a homogeneous medium with corresponding parameter space: the first case where L is the direction of rupture in the positive direction (L-POS) and the second case where L is in the direction of rupture in the negative direction (L-NEG).

[71] For the heterogeneous fault in a homogeneous medium: Table 3c shows V_L = 2.28 km/s, and Table 4a shows results for the bimaterial cases L-POS: V_L = 2.45 km/s and L-NEG: V_L = 2.27 km/s. Clearly these results show that for the bimaterial case the rupture in the positive direction (L-POS) is favored compared to the homogeneous case. Table 4b shows this comparison even more clearly for the bimaterial model with 25% contrast in shear wave speeds across the fault, where for the case L-POS: V_L = 2.51 km/s, and for the case L-NEG: V_L = 1.82 km/s. These results indicate that the rupture direction becomes more favored in the positive direction and less favored in the negative direction with increasing material contrast across the fault.

[72] Similarly to the homogeneous case we observed asymmetric bilateral rupture of the bimaterial fault with a heterogeneous coefficient of friction. The experimental results of *Xia et al.* [2005] also show that bilateral rupture with asymmetric rupture speeds for the positive and negative directions of a bimaterial fault. Likewise the numerical work by *Harris and Day* [2005] and *Andrews and Harris* [2005] report bilateral crack-like rupture propagation with a slight asymmetry in the rupture speeds for faults separating dissimilar materials. The laboratory experiments of *Xia et al.* [2005] allowed for controlled material contrasts and strain loading. They chose a relatively high material contrast of 25% in the shear wave speeds for their experiments. Like us, their results showed consistent bilateral rupturing of a bimaterial fault for a range of experimental parameters, where the ruptures propagated at different velocities in the different directions. They found that ruptures propagating in the positive direction propagated at the generalized Rayleigh wave speed, and ruptures in the opposite (negative) direction could propagate at subshear or supershear wave speeds. They were unable to identify if crack-like or pulse-like rupture propagation occurred.

[73] Several numerical studies by *Shi and Ben-Zion* [2006] and *Andrews and Ben-Zion* [1997] have demonstrated pulse-like behavior occurring for unilateral rupture propagation along bimaterial faults. In some cases *Shi and Ben-Zion* [2006] found bilateral rupture propagation could occur using a slip-weakening frictional model, and could proceed in either a crack-like or pulse-like fashion depending on the mechanical properties. In a recent paper, *Ampuero and Ben-Zion* [2007] showed that asymmetric bilateral pulse-like or crack-like rupture could also occur on a slip-rate weakening bimaterial fault, where on average the positive direction was favored for rupture propagation. We found that the rupture propagated bilaterally with different speeds in either the L or R direction (depending on both the spatial heterogeneity and material contrast across the fault) for both the bimaterial and homogeneous cases. We also found that the rupture speeds were influenced by the direction in the bimaterial case, with larger rupture speeds occurring in the positive direction when compared with the homogeneous model. This is in agreement with some of the laboratory experimental results of *Xia et al.* [2005] and the numerical results and geological
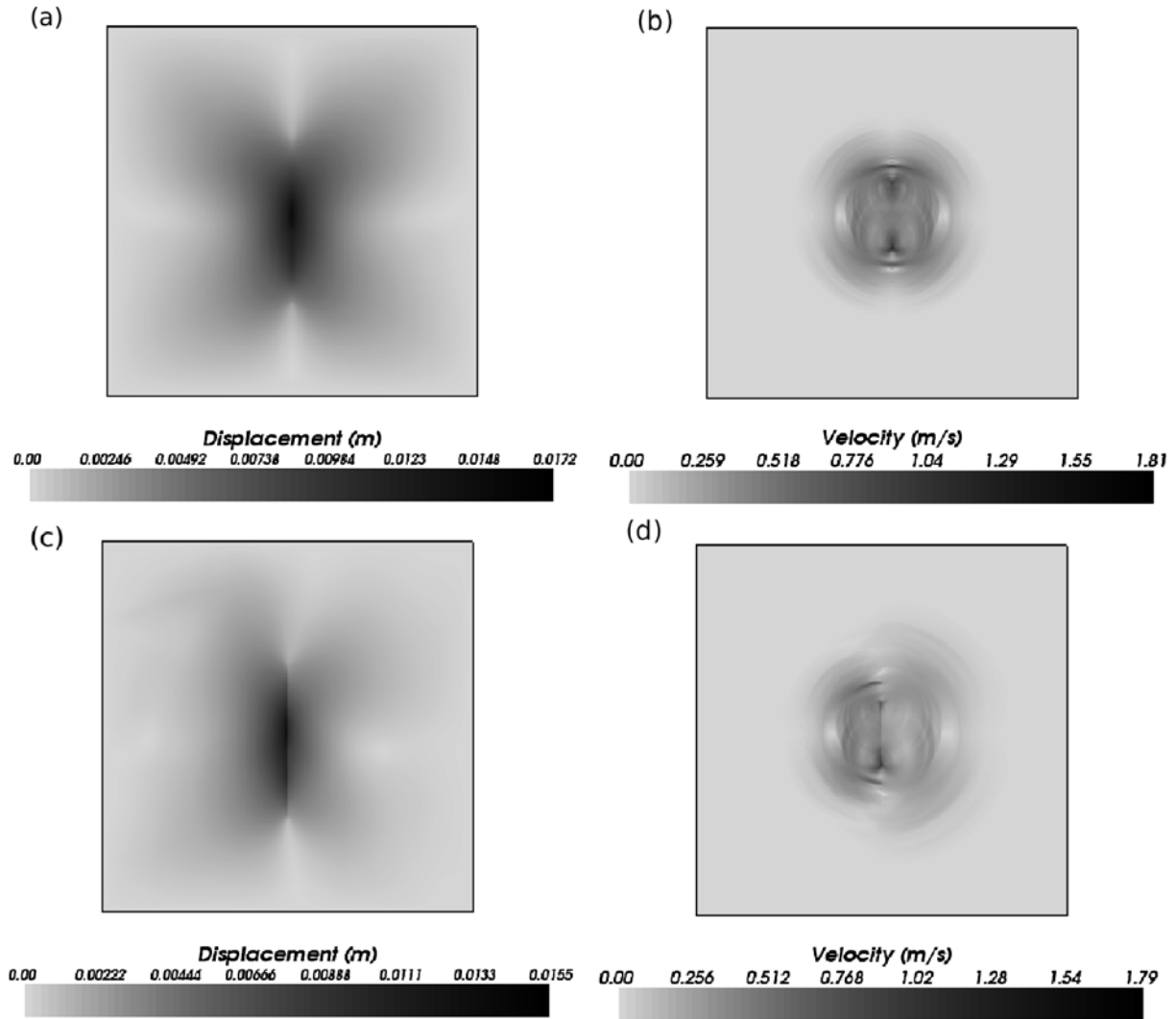
Figure 13. Plots of the displacement (absolute relative to initial) in Figures 13a and 13c at the end of the rupture for a heterogeneous fault in a homogeneous and bimaterial medium respectively, and velocity (absolute) at $t = 0.034$ s in Figures 13b and 13d for a heterogeneous fault in a homogeneous and bimaterial medium respectively. These plots use a Septic slip-weakening law for μ_{fric} and $\mu_d = 0.69 \; \mu_s$ where the bimaterial model has a 25% contrast in shear wave speeds across the fault and (for case L-POS).

observations made by *Harris and Day* [2005, 1997] and *Ampuero and Ben-Zion* [2007]. However, there is also some conflicting geological evidence from *Dor et al.* [2006] indicative of a preferred rupture direction where unilateral rupture propagation proceeded in the positive direction. We show in these two subsections that the positive direction is increasingly favored (and conversely for the negative direction) with increasing material contrast across the fault.

6.2. Rupture With 25% Contrast in the Shear Wave Speeds Across a Bimaterial Fault

[74] We repeated the simulations of the previous section for a bimaterial fault with a material contrast of 25% in the shear wave speeds of region 1 and region 2 (compared with 10% in the last section). We are modeling the same region as shown in Figure 12, but instead we use the following values for the Lamé coefficients for region 2: $\lambda_2 = \mu_2 = 52.9$ GPa and a density of $\rho_2 = 2.5$ g/cm^3. Thus the shear wave speed for region 2 is Vs = 4.6 km/s and the

compressional wave speed is $V_p = 7.97$ km/s. We apply strains of: $\epsilon_{00}^1 = -0.002$ and $\epsilon_{01}^1 = 0.0018$ ($\epsilon_{00}^2 = -0.001361$ and $\epsilon_{01}^2 = 0.001225$).

[75] Table 4b shows the results for a bimaterial fault with 25% contrast in the shear wave speeds across the fault. We investigated the difference between bimaterial fault rupture along in either the positive direction, (the direction of slip in the more compliant material), or in the negative direction. Because of the greater material contrast we note that the rupture in the positive direction in this case is highly preferred over rupture in the negative direction in comparison to the results with 10% material contrast.

[76] Figures 13a and 13b show the absolute displacement and absolute velocity respectively for a fault in a homogeneous medium. Figures 13c and 13d show similar plots for a bimaterial fault. Similarly to the numerical calculations of *Benzion* [2001] and *Andrews and Ben-Zion* [1997] we find that the displacement is greater for the more compliant
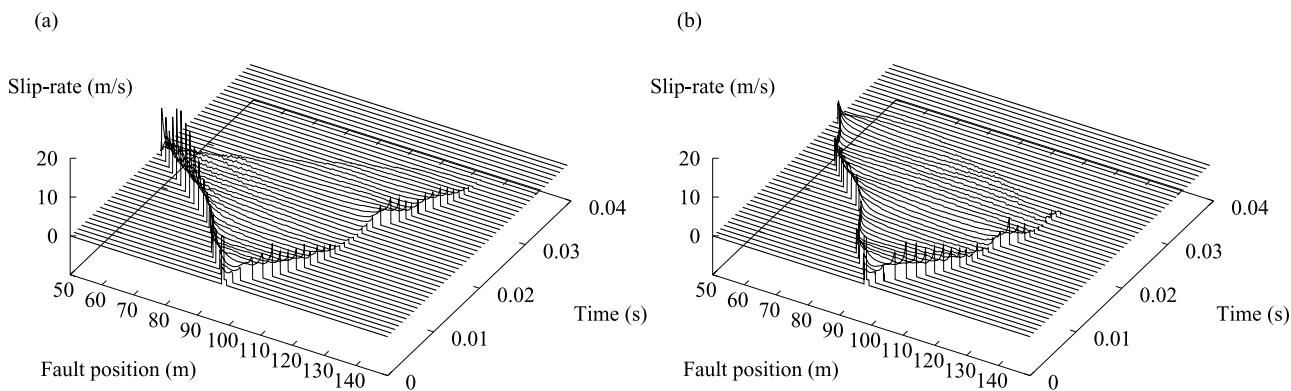
(a)

(b)

Figure 14. Time histories of the plastic slip-rate along the fault for the case studies *L*-POS and *L*-NEG in Figures 14a and 14b, respectively, for a bimaterial fault with 25% contrast in the shear wave speeds across the fault using a Septic slip-weakening law for μ_{fric} and $\mu_d = 0.69\ \mu_s$ and a mesh spacing of $\Delta x = 0.098$ m.

region (region 1) in the bimaterial fault model shown in Figure 13c. This is because the strain is greater in the more compliant material (region 1) than the stiffer material (region 2). Also we can observe in Figure 13d that the seismic waves traveling from the fault travel at a much greater speed (as expected) in region 2.

[77] Figure 14 compares the time history of the plastic slip-rate along the fault for the two cases studied: *L*-POS in (a) and *L*-NEG in (b). We can observe the effect of the material contrast where the left direction ($y = 100$ to 50 m) is favored (with higher slip velocities occurring) because it is the positive direction in (a) compared with (b) where it is in the negative direction. Both can be compared to the homogeneous case in Figure 9b. The effect of material contrast in the *R* direction where higher values of μ_s lock the fault is less pronounced, and all figures including the fault in a homogeneous medium show a decaying pulse in this direction. In Figure 14b we observe higher peak slip velocities initially in the *R* direction (positive) than the corresponding case in (a) with *R* in the negative direction.

[78] Similarly to the homogeneous case with the same parameters we observe in Figure 14a that the rupture propagates as a decaying pulse in the negative direction and a sustained pulse in the positive direction. This can be compared to the "Weertman" (decaying) pulse in the neg-

ative direction and sustained pulse in the positive direction shown by *Cochard and Rice* [2000] for bimaterial interfaces (see Figure 7). However, as we saw a similar behavior with the fault in a homogeneous medium in Figure 9b, whether or not a sustained or decaying pulse will be produced is also strongly dependent on the spatial heterogeneity of the fault.

[79] Figures 15a to 15c show the slip-rate, slip and shear stress respectively for a point on the fault at $y = 75$ m (25 m from the midpoint of the fault). We show these for a mesh spacing of either 0.098 m or 0.78 m to show the low level of numerical noise with both mesh sizes. Often bimaterial fault rupture models are ill-posed for a certain range of parameters whereby numerical solutions do not converge through grid size reduction. *Ranjith and Rice* [2001] showed that use of an experimentally based frictional law which incorporates a memory dependence, rather than an instantaneous dependence, on normal stress could provide regularization of this problem in the ill-posed range. Employment of our elastoplastic model implies a "memory" dependence in our frictional law where the fault has both an elastic and plastic response to the applied stress. All frictional laws we employed depend only on the plastic response (slip) of the fault, and as such the elastic component of the slip may provide a "memory" dependence through the elastic response of the fault. Table 4 shows that the bimaterial
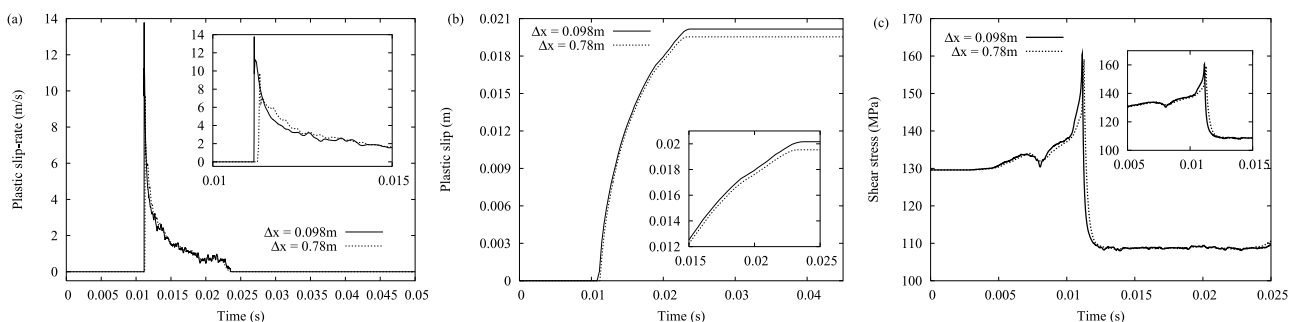
(a)

(b)

(c)

Figure 15. Time histories of the plastic slip-rate, plastic slip, and shear stress in Figures 15a, 15b, and 15c, respectively, for a point on the fault at a distance of approximately 25 m (at $y = 75$ m) from the midpoint on the fault for two mesh spacings: $\Delta x = 0.098$ m and 0.78 m. These plots were calculated for a Septic slip-weakening law for μ_{fric} and $\mu_d = 0.69\ \mu_s$ and using a bimaterial fault model with 25% contrast in the shear wave speeds across the fault (for case *L*-POS).

results converged with mesh size reduction for the range of material parameters we studied.

[80] Due to the huge parameter space that these calculations can afford, only a subset of the dynamical behavior that can be produced is shown here. Several researchers have addressed the question of whether material contrast can predict earthquake rupture direction [*Xia et al.*, 2005; *Harris and Day*, 2005; *Ampuero and Ben-Zion*, 2007; *Ben-Zion*, 2001]. We shed further light on this issue and demonstrate through our broad parameter study that rupture along bimaterial interfaces can exhibit a diversity of phenomena. Consistent with the experimental results of *Xia et al.* [2005] and numerical simulations of *Harris and Day* [2005, 1997]; *Ampuero and Ben-Zion* [2007], we found that rupture could propagate bilaterally along bimaterial faults. We found the material contrast influenced the favored rupture direction and the asymmetric nature of the displacement on either side of the interface, as in the theoretical work of *Ampuero and Ben-Zion* [2007]. However, we demonstrated that the material contrast is not the only important factor in determining the propagation direction, other factors such as the stress distribution and spatial heterogeneity along the fault were also instrumental.

7. Conclusions

[81] We demonstrate that more complex rupture characteristics can be produced with more strongly slip-weakening frictional laws. The more strongly slip-weakening laws we considered (Quintic and Septic) were able to produce pulse-like ruptures with more realistic rupture scaling properties. We demonstrate that pulse-like rupture can be produced using our modified slip-weakening frictional laws which include static restrengthening. Pulse-like formation in these models also depended on the weakness of the fault through the dynamic coefficient of friction. If the fault was too weak (low μ_d) crack-like ruptures only were produced, however when μ_d reached a critical value pulse-like rupture formation could occur. The degree of slip-weakening in the frictional law is very relevant to the mode and scale of rupture produced, and has to be finely tuned to reproduce realistic earthquake rupture characteristics.

[82] We demonstrate the applicability of our elastoplastic fault model for modeling dynamic rupture and wave propagation at a fault. We show results for homogeneous, heterogeneous and bimaterial fault systems. We have demonstrated the rich array of dynamic properties that can be simulated by varying different model parameters. These include: demonstration of either the crack-like or pulse-like nature of rupture propagation depending on the spatial heterogeneity and material contrast across the fault and the degree of slip-weakening in the frictional law, supershear and subshear rupture speeds depending primarily on the weakness of the fault, and asymmetric bilateral propagation of rupture along a bimaterial fault. We found that a Quintic slip-weakening law produced the most realistic RMS slips, RMS peak slip velocities and rupture velocities when compared to geological data [*Mai and Beroza*, 2000; *Heaton*, 1990; *Kanamori et al.*, 1998].

[83] The success of this work in modeling at least qualitatively many of the experimental observations made

by *Xia et al.* [2004, 2005], *Xia* [2005], and *Lykotrafitis et al.* [2006] attests to the usefulness and value in our theoretical approach. We demonstrate that the presence of spatial heterogeneities and material contrast across a fault combined with strongly slip-weakening friction can lead to pulse-like rupture occurring. Our numerical simulations also elucidate the asymmetric bilateral nature of rupture propagation along bimaterial faults, and provide further theoretical proof that bilateral rupture occurs readily at bimaterial faults and that the direction of rupture propagation is dependent upon more factors than just the material contrast at the interface. Our results indicate that while material contrast is not the only determining factor in preferred rupture direction, the positive direction is increasingly favored (and conversely for the negative direction) with increasing material contrast across the fault.

[84] Ongoing research is concentrated on modeling multiple earthquake cycles, which can permit fault systems with any number of faults with arbitrary geometry and mechanical properties [*Olsen-Kettle et al.*, 2007]. Our research goal is to provide comprehensive modeling of fault systems which can be applied to synthetic seismicity studies, seismic hazard assessment and earthquake forecasting.

References

Abercrombie, R. E., and J. R. Rice (2005), Can observations of earthquake scaling constrain slip weakening?, *Geophys. J. Int.*, *162*, 406–424.

Ampuero, J.-P., and Y. Ben-Zion (2007), Cracks, pulses and macroscopic asymmetry or dynamic rupture on a bimaterial interface with velocity-weakening friction, *Geophys. J. Int.*, doi:10.1111/j.1365-246X.2008.03736.x.

Anand, L. (1993), A constitutive model for interface friction, *Comput. Mech.*, *12*, 197–213.

Andrews, D. J. (1976), Rupture velocity of plane strain shear cracks, *J. Geophys. Res.*, *81*, 5679–5687.

Andrews, D. J. (1999), Test of two methods for faulting in finite difference calculations, *Bull. Seismol. Soc. Am.*, *89*, 931–937.

Andrews, D. J. (2002), A fault constitutive relation accounting for thermal pressurization of pore fluid, *J. Geophys. Res.*, *107*(B12), 2363, doi:10.1029/2002JB001942.

Andrews, D. J., and Y. Ben-Zion (1997), Wrinkle-like slip pulse on a fault between different materials, *J. Geophys. Res.*, *102*, 553–571.

Andrews, D., and R. A. Harris (2005), The wrinkle-like slip pulse is not important in earthquake dynamics, *Geophys. Res. Lett.*, *32*, L23303, doi:10.1029/2005GL023996.

Baumberger, T., F. Heslot, and B. Perrin (1994), Crossover from creep to inertial motion in friction dynamics, *Nature*, *367*, 544–546.

Ben-Zion, Y. (2001), Dynamic ruptures in recent models of earthquake faults, *J. Mech. Phys. Solids*, *49*, 2209–2244.

Cerjan, C., D. Kosloff, R. Kosloff, and M. Reshef (1985), A nonreflecting boundary condition for discrete acoustic and elastic wave equations, *Geophysics*, *50*, 705–708.

Chambon, G., J. Schmittbuhl, and A. Corfdir (2006), Frictional response of a thick gouge sample: 2. Friction law and implications for faults, *J. Geophys. Res.*, *111*, B09309, doi:10.1029/2004JB003339.

Cochard, C., and R. Madariaga (1994), Dynamic faulting under rate-dependent friction, *Pure Appl. Geophys.*, *142*, 419–445.

Cochard, A., and J. R. Rice (2000), Fault rupture between dissimilar materials: Ill-posedness, regularization and slip-pulse response, *J. Geophys. Res.*, *105*, 25,891–25,907.

Coker, D., G. Lykotrafitis, A. Needleman, and A. J. Rosakis (2005), Frictional sliding modes along an interface between identical elastic plates subject to shear impact loading, *J. Mech. Phys. Solids*, 53, 884–922.

Dalguer, L. A., and S. M. Day (2006), Comparison of fault representation methods in finite difference simulations of dynamic rupture, *Bull. Seismol. Soc. Am.*, 96, 1764–1778.

Day, S. M., L. A. Dalguer, N. Lapusta, and Y. Liu (2005), Comparison of finite difference and boundary integral solutions to three-dimensional spontaneous rupture, *J. Geophys. Res.*, 110, B12307, doi:10.1029/2005JB003813.

de Borst, R., and L. J. Sluys (2002), *Computational Methods in Non-Linear Solid Mechanics*, TUDelft Delft Univ. of Technol., Netherlands.

Dieterich, J. H. (1979), Modeling of rock friction: 1. Experimental results and constitutive equations, *J. Geophys. Res.*, 84, 2161–2168.

Dor, O., T. K. Rockwell, and Y. Ben-Zion (2006), Geological observations of damage asymmetry in the structure of the San Jacinto, San Andreas and Punchbosl faults in southern California: A possible indicator for preferred rupture direction, *Pure Appl. Geophys.*, 163, 301–349.

Festa, G., and J.-P. Vilotte (2006), Influence of the rupture initiation on the intersonic transition: Crack-like versus pulse-like modes, *Geophys. Res. Lett.*, 33, L15320, doi:10.1029/2006GL026378.

Gear, C. W. (1971), *Numerical Inital Value Problems in Ordinary Differential Equations*, Prentice-Hall, Englewood Cliffs, N. J.

Giannakopoulos, A. E. (1989), The return mapping method for the integration of friction constitutive relations, *Comput. Struct.*, 32, 157–167.

Gross, L., L. Bourgouin, A. J. Hale, and H.-B. Mühlhaus (2007), Interface modeling in incompressible media using level sets in escript, *Phys. Earth Planet. Inter.*, 163, 23–34.

Harris, R. A. (2004), Numerical simulations of large earthquakes: Dynamic rupture propagation on heterogeneous faults, *Pure Appl. Geophys.*, 161, 2171–2181.

Harris, R. A., and R. J. Archuleta (2004), Seismology: Earthquake rupture dynamics: Comparing the numerical simulation methods, *Eos Trans. AGU*, 85(34), 321, doi:10.1029/2004EO340003.

Harris, R. A., and S. M. Day (1997), Effects of a low-velocity zone on a dynamic rupture, *Bull. Seismol. Soc. Am.*, 87, 1267–1280.

Harris, R. A., and S. M. Day (2005), Material contrast does not predict earthquake rupture propagation direction, *Geophys. Res. Lett.*, 32, L23301, doi:10.1029/2005GL023941.

Heaton, T. H. (1990), Evidence for and implications of self-healing pulses of slip in earthquake rupture, *Phys. Earth Planet. Inter.*, 64, 1–20.

Ida, Y. (1972), Cohesive force across the tip of a longitudinal-shear crack and Griffith's specific surface energy, *J. Geophys. Res.*, 77, 3796–3805.

Kanamori, H., and E. E. Brodsky (2004), The physics of earthquakes, *Rep. Prog. Phys.*, 67, 1429–1496.

Kanamori, H., D. L. Anderson, and T. H. Heaton (1998), Frictional melting during the rupture of the 1994 Bolivian earthquake, *Science*, 279, 839–842.

Lachenbruch, A. H. (1980), Frictional heating, fluid pressure and the resistance to fault motion, *J. Geophys. Res.*, 85, 6097–6122.

Lapusta, N., and J. R. Rice (2003), Nucleation and early seismic propagation of small and large events in a crustal earthquake model, *J. Geophys. Res.*, 108(B4), 2205, doi:10.1029/2001JB000793.

Lapusta, N., J. R. Rice, Y. Ben-Zion, and G. Zheng (2000), Elastodynamic analysis for slow tectonic loading with spontaneous rupture episodes on faults with rate- and state-dependent friction, *J. Geophys. Res.*, 105, 765–789.

Laursen, T. A., and J. C. Simo (1993), A continuum-based finite element formulation for the implicit solution of multibody large deformation frictional contact problems, *Int. J. Numer. Methods Eng.*, 36, 3451–3485.

Lykotrafitis, G., and A. J. Rosakis (2006), Sliding along frictionally held incoherent interfaces in homogeneous systems subjected to dynamic shear loading: A photoelastic study, *J. Int. Fract.*, 140, 213–233.

Lykotrafitis, G., A. J. Rosakis, and G. Ravichandran (2006), Self-healing pulse-like shear ruptures in the laboratory, *Science*, 313, 1765–1768.

Madariaga, R., K. Olsen, and R. Archuleta (1998), Modeling dynamic rupture in a 3D earthquake fault model, *Bull. Seismol. Soc. Am.*, 88, 1182–1197.

Mai, P. M., and G. C. Beroza (2000), Source scaling properties from finite-fault-rupture models, *Bull. Seismol. Soc. Am.*, 90, 604–615.

Marone, C. (1998), Laboratory-derived friction laws and their application to seismic faulting, *Annu. Rev. Earth Planet. Sci.*, 26, 643–696.

Marone, C., and A. O. B. E. Hobbs (1992), Coulomb constitutive laws for friction: Contrasts in frictional behavior for distributed and localized shear, *Pure Appl. Geophys.*, 139, 195–214.

Mase, C. W., and L. Smith (1987), Effects of frictional heating on the thermal, hydrologic, and mechanical response of a fault, *J. Geophys. Res.*, 92, 6249–6272.

Michalowski, R., and Z. Mròz (1978), Associated and non-associated sliding rules in contact friction problems, *Arch. Mech.*, 30, 259–276.

Mora, P., and D. Place (1994), Simulation of the frictional stick-slip instability, *Pure Appl. Geophys.*, 143, 61–87.

Nielsen, S. B., and J. M. Carlson (2000), Rupture pulse characterization: Self-healing, self-similar, expanding solutions in a continuum model of fault dynamics, *Bull. Seismol. Soc. Am.*, 90, 1480–1497.

Olsen-Kettle, L. M., D. Weatherley, L. Gross, and H.-B. Mühlhaus (2007), Multicycle dynamics of fault systems and static and dynamic triggering of earthquakes, in *Proc. Aust. Earthquake Eng. Soc. Conf.* (Available at http://www.aees.org.au/)

Palmer, A. C., and J. R. Rice (1973), The growth of slip surfaces in the progressive failure of over-consolidated clay, *Proc. Roy. Soc., Ser. A and Ser. B*, 332, 527–548.

Perić, D., and D. R. J. Owen (1992), Computational model for 3-D contact problems with friction based on the penalty method, *Int. J. Numer. Methods Eng.*, 35, 1289–1309.

Povirk, G. L., and A. Needleman (1993), Finite element simulations of fiber pull-out, *J. Eng. Mater. Technol.*, 115, 286–291.

Press, W. H., S. A. Teukolsky, W. T. Vetterling, and B. P. Flannery (1992), *Numerical Recipes*, 2nd ed., Cambridge Univ. Press, Cambridge.

Radi, E., D. Bigoni, and A. Tralli (1999), On uniqueness for frictional contact rate problems, *J. Mech. Phys. Solids*, 47, 275–296.

Ranjith, K., and J. R. Rice (2001), Slip dynamics at an interface between dissimilar materials, *J. Mech. Phys. Solids*, 49, 341–361.

Rice, J. R. (2001), New perspectives on crack and fault dynamics, in *Mechanics for a New Millennium: Proc. 20th Int. Congr. Theor. Appl. Mech.*, edited by H. Aref and W. Phillips, pp. 1–23, Springer, Chicago, Ill.

Rice, J. R. (2006), Heating and weakening of faults during earthquake slip, *J. Geophys. Res.*, 111, B05311, doi:10.1029/2005JB004006.

Rice, J. R., and M. Cocco (2007), Seismic fault rheology and earthquake dynamics, in *Tectonic Faults Agents of Change on a Dynamic Earth*, edited by M. R. Handy, G. Hirth, and N. Hovius, MIT Press, Cambridge, Mass.

Rice, J. R., C. G. Sammis, and R. Parsons (2005), Off-fault secondary failure induced by a dynamic slip pulse, *Bull. Seismol. Soc. Am.*, 95, 109–134.

Rojas, O., S. Day, J. Castillo, and L. A. Dalguer (2008), Modeling of rupture propagation using high-order mimetic finite differences, *Geophys. J. Int.*, 172, 631–650.

Rosakis, A. J., O. Samudrala, and D. Coker (1999), Cracks faster than the shear wave speed, *Science*, 284, 1337–1340.

Ruina, A. (1983), Slip instability and state variable friction laws, *J. Geophys. Res.*, 84, 10,359–10,370.

Shi, Z., and Y. Ben-Zion (2006), Dynamic rupture on a bimaterial governed by slip-weakening friction, *Geophys. J. Int.*, 165, 469–484.

Shi, Z., Y. Ben-Zion, and A. Needleman (2008), Properties of dynamic rupture and energy partition in a solid with a frictional interface, *J. Mech. Phys. Solids*, 56, 5–24.

Taylor, J. R. (1982), *An Introduction to Error Analysis*, Univ. Sci. Books, Mill Valley, Calif.

Wibberley, C. A., and T. Shimamoto (2005), Earthquake slip weakening and asperities explained by thermal pressurization, *Nature*, 436, 689–692.

Wriggers, P. (2006), *Computational Contact Mechanics*, 2nd ed., Springer-Verlag, Berlin.

Wriggers, P., T. Vu Van, and E. Stein (1990), Finite element formulation of large deformation impact-contact problems with friction, *Comput. Struct.*, 37, 319–331.

Xia, K. (2005), Laboratory investigations of earthquake dynamics, Ph.D. thesis, Calif. Inst. of Technol., Pasadena, Calif. (Available at http://etd.caltech.edu/etd/available/etd-02262005-161824)

Xia, K., A. J. Rosakis, and H. Kanamori (2004), Laboratory earthquakes: The sub-Rayleigh-to-supershear rupture transition, *Science*, 303, 1859–1861.

Xia, K., A. J. Rosakis, H. Kanamori, and J. R. Rice (2005), Laboratory earthquakes along inhomogeneous faults: Directionality and supershear, *Science*, 308, 681–684.

Zheng, G., and J. R. Rice (1998), Conditions under which velocity-weakening friction allows a self-healing versus a cracklike mode of rupture, *Bull. Seismol. Soc. Am.*, 88, 1466–1483.

————————————

L. Gross, H.-B. Mühlhaus, L. M. Olsen-Kettle, E. Saez, D. Weatherley, and H. L. Xing, Earth Systems Science Computational Centre, The University of Queensland, Sir James Foots Building, St Lucia, Qld 4072, Australia. (l.kettle1@uq.edu.au)